# Solid-State NMR, Mössbauer, Crystallographic, and Density Functional Theory Investigation of Fe–O₂ and Fe–O₂ Analogue Metalloporphyrins and Metalloproteins[†]

**Nathalie Godbout, Lori K. Sanders, Renzo Salzmann,[‡] Robert H. Havlin,[§] Mark Wojdelski,[⊥] and Eric Oldfield\***

*Contribution from the Departments of Chemistry and Biophysics, University of Illinois at Urbana-Champaign, 600 South Mathews Avenue, Urbana, Illinois 61801*

*Received September 14, 1998. Revised Manuscript Received February 12, 1999*

**Abstract:** We have synthesized and studied via solid-state NMR, Mössbauer spectroscopy, single-crystal X-ray diffraction, and density functional theory the following Fe–O₂ analogue metalloporphyrins: Fe(5,10,15,20-tetraphenylporphyrinate) (nitrosobenzene)(1-methylimidazole); Fe(5,10,15,20-tetraphenylporphyrinate) (nitroso-benzene)(pyridine); Fe(5,10,15,20-tetraphenylporphyrinate)(4-nitroso-*N*,*N*-dimethylaniline)(pyridine); Fe-(2,3,7,8,12,13,17,18-octaethylporphyrinate) (nitrosobenzene)(1-methylimidazole) and Co(2,3,7,8,12,13,17,18-octaethylporphyrinate)(NO). Our results show that the porphyrin rings of the two tetraphenylporphyrins containing pyridine are ruffled while the other three compounds are planar: reasons for this are discussed. The solid-state NMR and Mössbauer spectroscopic results are well reproduced by the DFT calculations, which then enable the testing of various models of Fe–O₂ bonding in metalloporphyrins and metalloproteins. We find no evidence for two binding sites in oxypicket fence porphyrin, characterized by very different electric field gradients. However, the experimental Mössbauer quadrupole splittings can be readily accounted for by fast axial rotation of the Fe–O₂ unit. Unlike oxymyoglobin, the Mössbauer quadrupole splitting in PhNO•myoglobin does not change with temperature, due to the static nature of the Fe•PhNO subunit, as verified by ²H NMR of Mb•[²H₅]PhNO. Rotation of O₂ to a second (minority) site in oxymyoglobin can reduce the experimental quadrupole splittings, either by simple exchange averaging, or by an electronic mechanism, without significant changes in the Fe–O–O bond geometry, or a change in sign of the quadrupole splitting. DFT calculations of the molecular electrostatic potentials in CO, PhNO, and O₂-metalloporphyrin complexes show that the oxygen sites in the PhNO and O₂ complexes are more electronegative than that in the CO system, which strongly supports the idea that hydrogen bonding to O₂ will be a major contributor to O₂/CO discrimination in heme proteins.

## Introduction

The question of how O₂ binds to Fe atoms in respiratory proteins, and how CO is discriminated against binding, is a topic of continuing interest.[1] Here, both crystallographic[2–5] and spectroscopic methods, such as infrared/Raman spectroscopy,[6–8] nuclear magnetic resonance (NMR),[9–11] and Mössbauer spectroscopy,[12–15] have an important role to play, by providing basic structural–spectroscopic correlations. To date, most studies have focused on the binding of CO to metalloproteins and metalloporphyrins, but the topic of O₂ binding is at least as important, albeit generally more technically demanding to investigate due to the lower chemical stability of O₂-adducts and their decreased spectral sensitivity. These difficulties have

(1) Springer, B. A.; Sligar, S. G.; Olson, J. S.; Phillips, G. N. *Chem. Rev.* **1994**, *94*, 699–714. Slebodnick, C.; Ibers, J. A. *J. Biol. Inorg. Chem.* **1997**, *2*, 521–525.

(2) Shaanan, B. *J. Mol. Biol.* **1983**, *171*, 31–59.

(3) Nagi, K.; Luisi, B.; Shih, D.; Miyazaki, G.; Imai, K.; Poyart, C.; De Young, A.; Kwiatkowsky, L.; Noble, R. W.; Lin, S.-H.; Yu, N.-T. *Nature* **1987**, *329*, 858–860.

(4) Phillips, S. E. V. *Nature* **1978**, *273*, 247–248. Phillips, S. E. V. *J. Mol. Biol.* **1980**, *142*, 531–554.

(5) Phillips, S. E. V.; Schoenborn, B. P. *Nature* **1981**, *292*, 81–82.

(6) Lim, M.; Jackson, T. A.; Anfinrud, P. A. *Science* **1995**, *269*, 962–965. Lim, M.; Jackson, T. A.; Anfinrud, P. A. *J. Chem. Phys.* **1995**, *102*, 4355–4366.

(7) Hirota, S.; Li, T.; Phillips, G. N.; Olson, J. S.; Mukai, M.; Kitagawa, T. *J. Am. Chem. Soc.* **1996**, *118*, 7845–7846. Potter, W. T.; Tucker, M. P.; Houtchens, R. A.; Caughey, W. S. *Biochemistry* **1987**, *26*, 4699–4707.

(8) Li, X.-Y.; Spiro, T. G. *J. Am. Chem. Soc.* **1988**, *110*, 6024–6033. Ray, G. B.; Li, X.-Y.; Ibers, J. A.; Sessler, J. L.; Spiro, T. G. *J. Am. Chem. Soc.* **1994**, *116*, 162–176.

(9) Gerothanassis, I. P.; Momenteau, M.; Hawkes, G. E.; Barrie, P. J. *J. Am. Chem. Soc.* **1993**, *115*, 9796–9797. Gerothanassis, I. P.; Barrie, P. J.; Momenteau, M.; Hawkes, G. E. *J. Am. Chem. Soc.* **1994**, *116*, 11944–11949.

(10) Barrie, P. J.; Gerothanassis, I. P.; Momenteau, M.; Hawkes, G. E. *J. Magn. Reson.* **1995**, *108*, 185–188.

(11) Oldfield, E.; Lee, H. C.; Coretsopoulos, C.; Adebodun, F.; Park, K. D.; Yang, S.; Chung, J.; Phillips, B. *J. Am. Chem. Soc.* **1991**, *113*, 8680–8685.

(12) Kirchner, R. F.; Loew, G. H. *J. Am. Chem. Soc.* **1977**, *99*, 4639–4647.

(13) Maeda, Y.; Harami, T.; Morita, Y.; Trautwein, A.; Gonser, U. *J. Chem. Phys.* **1981**, *75*, 36–43. Gonser, U.; Maeda, Y.; Trautwein, A.; Parak, F.; Formanek, H. *Z. Naturforsch.* **1974**, *29B*, 241–244.

(14) Spartalian, K.; Lang, G.; Collman, J. P.; Gagne, R. R.; Reed, C. A. *J. Chem. Phys.* **1975**, *63*, 5375–5382.

(15) Debrunner, P. G. In *Iron Porphyrins*; Lever, A. B. P., Gray, H. B., Eds.; VCH Publishers: New York, 1989; pp 139–234. Boso, B.; Debrunner, P. G.; Wagner, G. C.; Inubushi, T. *Biochim. Biophys. Acta* **1984**, *791*, 244–251.

resulted in the use of a wide range of Fe−O₂ analogues, such as CoNO,[16,17] FeRNO,[18,19] and CoO₂[20,21] complexes, for NMR, IR, Mössbauer, and electron spin resonance (ESR) investigations. A major goal of many of these studies is to obtain a better understanding of the geometric and electronic structures of relatively simple metal−ligand complexes, and then to extend these ideas to metalloproteins.

Quantum chemical methods[22−27] should, in principle, be able to help solve such problems, but a major difficulty is that the resolution of both protein crystal and solution structures is often insufficient to enable highly accurate calculations. This situation is beginning to improve with the development of intense synchrotron light sources for X-ray crystallography,[28,29] which together with the application of chemical shift,[30−32] chemical shift anisotropy,[33] and dipolar splitting[34−36] restraints in solution NMR spectroscopy can be expected to result in protein structures of significantly improved accuracy. But before quantum chemical methods are generally applied to investigating ligand binding

in proteins, they still need to be validated on smaller, more well characterized model systems. Then, it should be possible to refine both protein backbone and protein side-chain, as well as metal−ligand binding site structures, and to probe in detail electronic and electrostatic structures by use of quantum chemistry. For example, once a structure is known, it now appears to be possible to deduce charge densities ($\rho(\mathbf{r})$), electrostatic potentials ($\Phi(\mathbf{r})$), electric field gradients ($\nabla \cdot E$), and so forth from the experimental structures, which are in good accord with the results of quantum chemical calculations.[37−39]

In this article, we present results on the synthesis, structure, solid-state NMR, Mössbauer, and quantum chemical (density functional theory, DFT) investigations of a series of Fe−O₂-analogue metalloporphyrins, containing the groups Fe•RNO (HNO≡O₂) and CoNO. The ability to compute the spectroscopic observables gives some confidence in the quality of the DFT calculations, which are then used to investigate the topic of Fe−O₂ bonding in metalloporphyrins and metalloproteins.

The RNO analogues of heme proteins have been known for many years, primarily due to the fact that nitrobenzene poisoning[40] is due to the reduction of PhNO₂ to PhNHOH, which binds (as PhNO) to metHb to form Hb•PhNO.[41] Indeed, PhNO binds so strongly to Hb and Mb that it displaces even CO.[41] We have synthesized and characterized a range of Fe•RNO adducts, some of which display pronounced porphyrin ruffling, and we report the solid-state NMR and Mössbauer spectra of these systems. We then show that modern DFT methods enable prediction of not only their NMR spectra but also their ⁵⁷Fe Mössbauer spectra as well. These results validate use of the DFT method on oxyheme analogue models, and encourage an extrapolation to the FeO₂ systems, oxypicket fence porphyrin and oxymyoglobin, whose Mössbauer spectra have been the topic of debate for some time.[15] Our results with picket fence porphyrin supports a fast axial diffusion model for averaging of the electric field gradient, while a more restricted motion is suggested to be the origin of the large temperature dependence of the ⁵⁷Fe MbO₂ results, although alternative explanations are possible in the latter case. With PhNO bound to Mb, the experimental ⁵⁷Fe Mössbauer spectra are essentially temperature insensitive, a very different effect to that seen with MbO₂. With the isoelectronic CoNO complex, fast axial motion is hindered at low temperatures, plus, we predict and find an undistorted metalloporphyrin with a ∠Co−N−O of ∼120°, as deduced by crystallography, NMR, and via quantum chemical geometry optimization, essentially the same value as that for MbO₂ in the most recent structure determinations.[42] Since we find good agreement between the results of calculations and experiment for the chemical shieldings and shielding tensors, as well as for the electric field gradient

(16) Scheidt, W. R.; Hoard, J. L. *J. Am. Chem. Soc.* **1973**, *95*, 8281−8288. Ellison, M. K.; Scheidt, W. R. *Inorg. Chem.* **1998**, *37*, 382−383.

(17) Richter-Addo, G. B.; Hodge, S. J.; Yi, G.-B.; Khan, M. A.; Ma, T.; Van Caemelbecke, E.; Guo, N.; Kadish, K. M. *Inorg. Chem.* **1996**, *35*, 6530−6538; **1997**, *35*, 2696.

(18) Mansuy, D.; Battioni, P.; Chottard, J.-C.; Riche, C.; Chiaroni, A. *J. Am. Chem. Soc.* **1983**, *105*, 455−463.

(19) Gans, P.; Regnard, J. R.; Battioni, P.; Mansuy, D. *Chem. Phys.* **1980**, *45*, 401−408.

(20) Lee, H. C.; Peisach, J.; Dou, Y.; Ikeda-Saito, M. *Biochemistry* **1994**, *33*, 7609−7618. Lee, H. C.; Peisach, J.; Tsuneshige, A.; Yonetani, T. *Biochemistry* **1995**, *34*, 6883−6891.

(21) Hori, H.; Ikeda-Saito, M.; Yonetani, T. *J. Biol. Chem.* **1982**, *257*, 3636−3642. Miller, L. M.; Chance. M. R. *Biochemistry* **1995**, *34*, 10170−10179.

(22) Strohmeier, M.; Orendt, A. M.; Facelli, J. C.; Solum, M. S.; Pugmire, R. J.; Parry, R. W.; Grant, D. M. *J. Am. Chem. Soc.* **1997**, *119*, 7114−7120.

(23) Frisch, M. J.; Trucks, G. W.; Schlegel, H. B.; Gill, P. M. W.; Johnson, B. G.; Robb, M. A.; Cheeseman, J. R.; Keith, T.; Petersson, G. A.; Montgomery, J. A.; Raghavachari, K.; Al-Laham, M. A.; Zakrzewski, V. G.; Ortiz, J. V.; Foresman, J. B.; Cioslowski, J.; Stefanov, B. B.; Nanyakkara, A.; Challacombe, M.; Peng, C. Y.; Ayala, P. Y.; Chen, W.; Wong, M. W.; Andres, J. L.; Replogle, E. S.; Gomperts, R.; Martin, R. L.; Fox, D. J.; Binkley, J. S.; Defrees, D. J.; Baker, J.; Stewart, J. P.; Head-Gordon, M.; Gonzalez, C.; Pople, J. A.; GAUSSIAN 94, Revision E.2; Gaussian, Inc.: Pittsburgh, PA, 1997.

(24) Pulay, P.; Hinton, J. F.; Wolinski, K. In *Nuclear Magnetic Shieldings and Molecular Structure*; Tossell, J. A., Ed.; Kluwer Academic Publishers: The Netherlands, 1993; pp 243−262.

(25) Schreckenbach, G.; Ziegler, T. *J. Phys. Chem.* **1995**, *99*, 606−611.

(26) Malkin, V. G.; Malkina, O. L.; Casida, M. E.; Salahub, D. R. *J. Am. Chem. Soc.* **1994**, *116*, 5898−5908; Kaupp, M.; Malkin, V. G.; Malkina, O. L.; Salahub, D. R. *J. Am. Chem. Soc.* **1995**, *117*, 1851−1852; **1995**, *117*, 8492. Malkin, V. G.; Malkina, O. L.; Salahub, D. R. *Chem. Phys. Lett.* **1993**, *204*, 87−95.

(27) Rovira, C.; Ballone, P.; Parrinello, M. *Chem. Phys. Lett.* **1997**, *271*, 247−250. Rovira, C.; Kunc, K.; Hutter, J.; Ballone, P.; Parrinello, M. *J. Phys. Chem.* **1997**, *101*, 8914−8925.

(28) Sevcik, J.; Dauter, Z.; Lamzin, V. S.; Wilson, K. S. *Acta Crystallogr.* **1996**, *D52*, 327−344.

(29) Schlichting, I.; Berenden, J.; Phillips, G. N., Jr.; Sweet, R. M. *Nature* **1994**, *371*, 808−812. Teng, T.-Y.; Srajer, V.; Moffat, K. *Nature Struct. Biol.* **1994**, *1*, 701−705. Hartmann, H.; Zinser, S.; Komininos, P.; Schneider, R. T.; Nienhaus, G. U.; Parak, F. *Proc. Natl. Acad. Sci. U.S.A.* **1996**, *93*, 7013−7016.

(30) Ösapay, K.; Theriault, Y.; Wright, P. E.; Case, D. A. *J. Mol. Biol.* **1994**, *244*, 183−197. Ösapay, K.; Case, D. A. *J. Biomol. NMR* **1994**, *4*, 215−230.

(31) Pearson, J. G.; Wang, J.-F.; Markley, J. L.; Le, H.; Oldfield, E. *J. Am. Chem. Soc.* **1995**, *117*, 8823−8829.

(32) Kuszewski, J.; Qin, J.; Gronenborn, A. M.; Clore, G. M. *J. Magn. Reson.* **1995**, *106*, 92−96.

(33) Tjandra, N.; Bax, A. *J. Am. Chem. Soc.* **1997**, *119*, 9576−9577.

(34) Tjandra, N.; Bax, A. *Science* **1997**, *278*, 1111−1114.

(35) Tolman, J. R.; Flanagan, J. M.; Kennedy, M. A.; Prestegard, J. H. *Proc. Natl. Acad. Sci. U.S.A.* **1995**, *92*, 9279−9283.

(36) Clore, G. M.; Gronenborn, A. M.; Tjandra, N. *J. Magn. Reson.* **1998**, *131*, 159−162. Tjandra, N.; Omichinski, J. G.; Gronenborn, A. M.; Clore, G. M.; Bax, A. *Nature Struct. Biol.* **1997**, *4*, 732−738.

(37) Koritsánszky, T.; Flaig, R.; Zobel, D.; Krane, H.-G.; Morgenroth, W.; Luger, P. *Science* **1998**, *279*, 356−358.

(38) Flaig, R.; Koritsánszky, T.; Zobel, D.; Luger, P. *J. Am. Chem. Soc.* **1998**, *120*, 2227−2238.

(39) Bader, R. F. W. *Atoms in Molecules—a Quantum Theory*; Oxford University Press: Oxford, 1990.

(40) Filehne, W. *Arch. Exptl. Pathol. Pharmakol.* **1898**, *9*, 329. Loeb, R. F.; Bock, A. V.; Fitz, R. *Am. J. Med. Sci.* **1921**, *539*, 539.

(41) Keilin, D.; Hartree, E. F. *Nature* **1943**, *151*, 390−391. Murayama, M. *J. Biol. Chem.* **1960**, *235*, 1024−1028. Gibson, Q. H. *Biochem. J.* **1960**, *77*, 519−526.

(42) Carver, T. E.; Brantley, R. E., Jr.; Singleton, E. W.; Arduini, R. M.; Quillin, M. L.; Phillips, G. N., Jr.; Olson, J. S. *J. Biol. Chem.* **1992**, *267*, 14443−14450. See also: Abola, E. E.; Bernstein, F. C.; Bryant, S. H.; Koetzle, T. F.; Weng, J. Protein Data Bank. In *Crystallographic Databases-Information Content, Software Systems, Scientific Applications*, Allen, F. H., Bergerhoff, G., Sievers, R., Eds.; Data Commission of the International Union of Crystallography: Bonn/Cambridge/Chester, 1987; pp 107−132. Bernstein, F. C.; Koetzle, T. F.; Williams, G. J. B.; Meyer, E. F., Jr.; Brice, M. D.; Rodgers, J. R.; Kennard, O.; Shimanouchi, T.; Tasumi, M. *J. Mol. Biol.* **1977**, *112*, 535−542.

tensors of the metals, which implies a good description of both ground and excited states, we then briefly explore the question of the electrostatic structure of the FeCO, FeRNO, and $FeO_2$-metalloporphyrins, of particular interest in the context of hydrogen-bonding and $CO/O_2$ discrimination in heme proteins.[1]

## Experimental Section

**Synthetic Aspects.** All syntheses were carried out by using Schlenk techniques, as described elsewhere.[18,43]

**Fe(5,10,15,20-tetraphenylporphyrinate)(nitrosobenzene)-(pyridine)** was prepared by the NaBH₄ reduction of Fe(TPP)Cl in THF under Ar. The Fe(TPP)(THF)₂ was then converted to Fe(TPP)(py)₂ with pyridine, then 1.2 equiv of PhNO (as the dimer) added to form Fe-(TPP)(PhNO)(py). Crystallization was from a layered toluene/heptane system with a yield of 84%. Fe(TPP)(PhNO)(py)•0.5toluene Anal. data Calculated (Found): C, 78.00 (77.71); H, 4.70 (4.81); N, 9.32 (9.10).

**Fe(5,10,15,20-tetraphenylporphyrinate)(4-nitroso-*N*,*N*-dimethylaniline)(pyridine)** was prepared basically as described above except for the addition of 1.2 equiv of 4-nitroso-*N*,*N*-dimethylaniline (NODMA). Crystallization was from toluene/heptane with a yield of 80%. Fe(TPP)(NODMA)(py)•toluene: Anal. data Calculated (Found): C, 77.64 (77.16); H, 5.19 (4.93); N, 9.90 (10.21).

**Fe(5,10,15,20-tetraphenylporphyrinate)(nitrosobenzene)(1-methylimidazole)** was prepared basically as described above except for the addition of 1.2 equiv of PhNO (as the dimer) to Fe(TPP)(1-MeIm)₂. Crystallization was from toluene/pentane with a yield of 56%. Fe(TPP)-(PhNO)(1-MeIm): Anal. data Calculated (Found): C, 75.61 (75.69); H, 4.58 (4.50); N, 11.42 (11.27).

**Fe(2,3,7,8,12,13,17,18-octaethylporphyrinate)(nitrosobenzene)(1-methylimidazole)** was prepared basically as described above except for the use of Fe(OEP)Cl.

**Co(2,3,7,8,12,13,17,18-octaethylporphyrinate)(NO) and Co-(5,10,15,20-tetraphenylporphyrinate)(NO)** were both prepared with use of standard literature procedures.[44] [¹⁵NO] labeled OEP and TPP and [N¹⁷O] labeled OEP derivatives were prepared from K¹⁵NO₂ (Cambridge Isotopes, Andover, MA) or by the H₂¹⁷O exchange of KNO₂, to generate the appropriate isotopically enriched species.[45] For the OEP preparation, particular attention needs to be given to rigorous O₂ exclusion since any NO₂ generated can attach to the porphyrin meso carbons.[46] All compounds had satisfactory microanalyses for C, H, and N, and were further characterized by a strong IR band (in KBr) corresponding to the N—O stretching frequency: Co(TPP)NO, 1697 cm⁻¹; Co(OEP)NO, 1675 cm⁻¹.

**([⁵⁷Fe]-myoglobin)(PhNO) and Fe(myoglobin)([²H₅]-PhNO).** ([⁵⁷Fe]-myoglobin)(PhNO) was prepared from *met*-[⁵⁷Fe] myoglobin, whose synthesis was reported previously,[47] by addition of PhNHOH, prepared by the Zn reduction of PhNO₂.[48] The phenylhydroxylamine is thought to be oxidized by the ferric iron to PhNO,[41] which then binds to the reduced Mb to give the desired product. The ([⁵⁷Fe]-myoglobin)(PhNO) was purified over Sephadex G-25, concentrated on an Amicon ultrafiltration apparatus, then frozen for Mössbauer spectroscopy. The [²H₅]-nitrosobenzene adduct was prepared in basically the same manner, except that [²H₅]-PhNO₂ (Cambridge Isotope Laboratories) was used to generate the required [phenyl-²H₅]-PhNHOH, and the product was crystallized from concentrated (NH₄)₂SO₄(aq).

**Nuclear Magnetic Resonance Spectroscopy.** Solution-state NMR spectra were recorded by using a Varian (Palo Alto, CA) Unity Plus 500 MHz instrument. Solid-state ¹⁵N and ¹⁷O "magic-angle" sample-spinning (MAS) NMR spectra were obtained by using 360, 500, and 600 MHz (¹H) "home-built" spectrometers, which consist of Oxford Instruments (Oxford, UK) 8.45 T/3.5 in., 11.7 T/2.0 in. and 14.1 T/2.0

in. bore superconducting solenoid magnets, Tecmag (Houston, TX) Aries and Libra pulse programmers, Doty Scientific (Columbia, SC) 5 mm MAS NMR probes and spin-speed controllers, and a variety of other home-built digital and radio frequency circuitries.

**Mössbauer Spectroscopy.** Mössbauer spectra were recorded by using a Ranger Scientific, Inc. (Burleson, TX) MS-900 spectrometer equipped with a VT-900 transducer and a Kr—CO₂ gas proportional counter. The source was ⁵⁷Co in a 6 μm rhodium foil having an 8 mm active diameter, and an initial activity of 25 mCi (Amersham Life Sciences, Arlington Heights, IL). Low temperatures were obtained by using a Janis Research Company, Inc. (Wilmington, MA) cryostat. Samples were sealed in thin Delrin containers with epoxy resin.

**X-ray Crystallography.** Crystals were mounted with oil (Paratone-N, Exxon) to thin glass fibers and diffraction data collected on a Bruker (Madison, WI) SMART/CCD diffractometer using Mo Kα radiation ($\lambda = 0.71073$ Å). Structures were solved by using SHELXTL V5.0 (Bruker) software. Space group choice was confirmed by successful convergence of full-matrix least-squares refinements on $F^2$. Hydrogen atoms were assigned idealized locations and given isotropic thermal parameter 1.2 times the thermal parameter of the atom to which they were attached. Data were corrected for Lorentz and polarization effects and empirical absorption corrections were applied.

The color and morphology of the crystals, the crystallographic systems, and space groups, as well as other information related to the crystal structure determinations, are summarized in Table 1. In general, from 7459 to 26755 data points were collected with the area detector, and from 3761 to 11388 data points having $I > 2\sigma(I)$ were used in the refinements. The final $R_1$ values varied from 0.039 to 0.096, and the GOF values varied from 0.936 to 1.178, Table 1 (see also Supporting Information). Atomic coordinates, bond lengths, angles, and thermal parameters have also been deposited with the Cambridge Crystallographic Data Centre (CCDC). Any request to the CCDC for this material should quote the full literature citation and the reference number.

**Computational Aspects.** All chemical shielding, electric field gradient, and geometry optimization calculations were carried out by using density functional theory as embodied in Gaussian-94.[23] As described in detail in several recent articles,[43,49,50] it is now possible to compute both ligand and metal shieldings, as well as ligand and metal electric field gradients, in a variety of metalloporphyrins, with good accord being found between theory and experiment. Typically, we have used moderately sized, locally dense basis sets such as Wachters' all electron basis (14s11p6d/8s7p4d)[51,52] for iron together with 6-311++G(2d) for those atoms coordinated to iron, and other atoms (e.g., O in CO) of particular interest, while smaller (6-31G*, 3-21G*) basis sets are used on the more distant atoms. This approach enables relatively rapid property predictions with no perceptible increase in error over larger, more uniform basis calculations. The gauge-including atomic orbitals method[53] was used for the chemical shielding calculations, with Becke's exchange functional and Perdew and Wang's gradient-corrected correlation functional (BPW91).[54] For the metal electric field gradients, we employed Becke's three-parameter functional[55] with a nonlocal correlation term given by the Lee, Yang, and Parr expression,[56] the

(48) Vogel, A. I. *A Text-Book of Practical Organic Chemistry*; Longmans, Green and Co. Ltd.: London, 1964; pp 630−631.

(49) Havlin, R. H.; Godbout, N.; Salzmann, R.; Wojdelski, M.; Arnold, W.; Schulz, C. E.; Oldfield, E. *J. Am. Chem. Soc.* **1998**, *120*, 3144−3151.

(50) Godbout, N.; Havlin, R.; Salzmann, R.; Debrunner, P. G.; Oldfield, E. *J. Phys. Chem.* **1998**, *102*, 2342−2350.

(51) Wachters, A. J. H. *J. Chem. Phys.* **1970**, *52*, 1033−1036. Wachters, A. J. H. *IBM Technol. Rep.* 1969.

(52) Basis sets were obtained from the Extensible Computational Chemistry Environment Basis Set Database, Version 1.0, as developed and distributed by the Molecular Science Computing Facility, Environmental and Molecular Sciences Laboratory, which is part of the Pacific Northwest Laboratory, P.O. Box 999, Richland, WA 99352, and is funded by the U.S. Department of Energy under contract DE-AC06-76RLO 1830. Contact David Feller, Karen Schuchardt, or Don Jones for further information.

(53) Ditchfield, R. *Mol. Phys.* **1974**, *27*, 789−807.

(54) Becke, A. D. *Phys. Rev. A* **1988**, *38*, 3098−3100. Perdew, J. P.; Wang, Y. *Phys. Rev. B* **1992**, *45*, 13244−13249.

(55) Becke, A. D. *J. Chem. Phys.* **1993**, *98*, 5648−5652.

(56) Lee, C.; Yang, W.; Parr, R. G. *Phys. Rev. B* **1988**, *37*, 785−789.

(43) Salzmann, R.; Ziegler, C. J.; Godbout, N.; McMahon, M.; Suslick, K. S.; Oldfield, E. *J. Am. Chem. Soc.* **1998**, *120*, 11323−11334.

(44) Scheidt, W. R.; Hoard, J. L. *J. Am. Chem. Soc.* **1973**, *95*, 8281−8288.

(45) Schenk, P. W. *Handbook of Preparative Inorganic Chemistry* **1963**, *1*, 460−464.

(46) Fanning, J. C.; Mandel, F. S.; Gray, T. L. *Tetrahedron* **1979**, *35*, 1251−1255.

(47) Lee, H. C.; Gard, J. K.; Brown, T. L.; Oldfield, E. *J. Am. Chem. Soc.* **1985**, *107*, 4087−4088.

**Table 1.** Crystallographic Data Summary

| | Fe(TPP)(PhNO)(py) | Fe(TPP)(NODMA)(py) | Fe(TPP)(PhNO)(1-MeIm) | Fe(OEP)(PhNO)(1-MeIm) | Co(OEP)(NO) |
|---|---|---|---|---|---|
| formula | $C_{55}H_{38}N_6OFe{\cdot}0.5$ toluene | $C_{57}H_{43}N_7OFe{\cdot}$toluene | $C_{54}H_{39}N_7OFe$ | $C_{46}H_{55}N_7OFe$ | $C_{36}H_{44}N_5OCo$ |
| formula weight | 900.83 | 989.97 | 857.77 | 777.82 | 621.69 |
| color | black | purple | purple/black | black | black |
| crystal system | triclinic | orthorhombic | triclinic | triclinic | triclinic |
| $a$ (Å) | 11.904(11) | 38.8181(13) | 10.779(2) | 13.67950(10) | 10.4844(6) |
| $b$ (Å) | 13.259(12) | 12.3091(4) | 17.829(3) | 13.9290(3) | 10.6084(7) |
| $c$ (Å) | 16.452(2) | 21.4098(7) | 22.728(4) | 23.1320(6) | 14.0904(9) |
| $\alpha$ (deg) | 87.525(2) | 90 | 103.220(4) | 72.4130(10) | 79.7580(10) |
| $\beta$ (deg) | 70.489(2) | 90 | 93.811(4) | 73.5480(10) | 89.3980(10) |
| $\gamma$ (deg) | 70.556(2) | 90 | 97.839(4) | 84.640(2) | 80.2540(10) |
| $V$ (Å³) | 2301.3(4) | 10239.6(11) | 4190.6(13) | 4029.43(14) | 1519.6(2) |
| $Z$ | 2 | 8 | 4 | 4 | 2 |
| $D_{calc}$ (g cm⁻³) | 1.30 | 1.284 | 1.36 | 1.282 | 1.359 |
| space group | $P\bar{1}$ | $Iba2$ | $P\bar{1}$ | $P\bar{1}$ | $P\bar{1}$ |
| radiation, wavelength (Å) | Mo Kα, 0.71073 Å | Mo Kα, 0. 71073 Å | Mo Kα, 0. 71073 Å | Mo Kα, 0. 71073 Å | Mo Kα, 0. 71073 Å |
| $\mu$ (mm⁻¹) | 0.377 | 0.346 | 0.411 | 0.419 | 0.603 |
| crystal size (mm) | 0.08 × 0.19 × 0.22 | 0.10 × 0.24 × 0.36 | 0.08 × 0.24 × 0.30 | 0.40 × 0.16 × 0.14 | 0.16 × 0.19 × 0.20 |
| temp (K) | 198(2) | 198(2) | 198(2) | 198(2) | 198(2) |
| diffractometer | Bruker SMART/CCD | Bruker SMART/CCD | Bruker SMART/CCD | Bruker SMART/CCD | Bruker SMART/CCD |
| no. of data points collected | 13404 | 26755 | 17184 | 22373 | 7459 |
| no. of data points: $I > 2\sigma(I)$ | 3761 | 4388 | 3981 | 11388 | 4687 |
| abs min/max | 0.849/0.940 | 0.966/0.898 | 0.880/0.970 | 0.338/0.291 | 0.374/0.412 |
| $R_1$[a] (obsd data) | 0.063 | 0.062 | 0.096 | 0.059 | 0.039 |
| $wR_2$ $(a,b)$[b] | 0.080 (0.010, 0.0) | 0.146 (0.055, 0.0) | 0.173 (0.03, 0.0) | 0.135 (0.071, 0.0) | 0.082 (0.034, 0.687) |
| GOF[c] | 0.939 | 1.043 | 1.178 | 0.936 | 1.033 |

[a] $R1 = \Sigma(||F_o| - |F_c||)/\Sigma(|F_o|)$. [b] $wR_2 = [\Sigma[w(F_o^2 - F_c^2)^2]/\Sigma[w(F_o^2)^2]]^{1/2}$ where $w = 1/[\sigma^2(F_o^2) + (a*P)^2 + b*P]$ and $P = (F_o^2 + 2F_c^2)/3$. [c] GOF $= S = [\Sigma[w(F_o^2 - F_c^2)^2]/(n - p)]$, where $n =$ the number of reflections and $p =$ the total number of parameters refined.

B3LYP hybrid exchange-correlation functional. This approach has been used by us previously to successfully predict metal ion electric field gradients (EFGs, deduced experimentally from the ⁵⁷Fe Mössbauer quadrupole splittings) in 14 organometallic and heme-model compounds.[49] The use of two different functionals may appear unusual, but Bühl has shown that (⁵⁷Fe) metal shieldings are very accurately computed by using the B3LYP functional,[57] which therefore led us to use his approach to compute both metal shieldings as well as metal quadrupole splittings[49,50] in model heme systems.[50] However, we have previously noted that the B3LYP functional appears to overestimate the paramagnetic shifts of **ligand** atoms somewhat, especially for highly deshielded groups,[58] so for accuracy and consistency, we carried out separate calculations for ligand and metal properties.

In most cases, the structures employed were those determined crystallographically in this paper, but, as described previously, with the bulky ring substituents replaced by hydrogen.[49,50] In the case of CoNO, we also carried out a partial geometry optimization of the CoNO fragment (lanl2dz ECP and basis set/6-31G(d)/3-21G(d)/B3LYP) in which $d$(Co–N), d(N–O), the four $d$($N_{por}$–Co), $\angle$Co–N–O, the four $\angle N_{por}$–Co–$N_{NO}$, and the four $\angle N_{por}$–Co–N–O dihedral angles were left unconstrained. For the heme-$O_2$ calculations, we initially investigated planar porphyrin macrocycles having a variety of geometries,[43,59–61] using the bond lengths and bond angles reported for oxypicketfence porphyrin.[60] We then carried out a more systematic investigation of the ⁵⁷Fe electric field gradient using six porphyrins containing a planar macrocycle,[59] in which the orientations of the oxygen and imidazole base were systematically varied in order to map out a wide range of possible bonding situations, as discussed in detail in the text. In one set of calculations, we utilized a planar metallocycle and the $FeO_2$ bond lengths and angles were fixed or unoptimized, while in a second set of calculations we carried out a partial geometry optimization ($d$(Fe–O), $d$(O–O), $\angle$Fe–O–O) of the $FeO_2$ unit at B3LYP. In a third set of

calculations, we utilized a ruffled metallocycle, and used fixed bond lengths and angles (since there was essentially no difference seen between the first two sets of calculations). Selected bond lengths, bond angles, and torsion angles (i.e., proximal base orientations) used in the calculations are given for convenience in Table 2. We also evaluated the charge densities $\rho(\mathbf{r})$ and the molecular electrostatic potentials, $\Phi$-$(\mathbf{r})$, using both BPW91 and B3LYP XC functionals. These G94 results were displayed in Cerius2 (Molecular Simulations Inc., San Diego, CA). We also carried out a series of semiempirical molecular mechanics calculations (Spartan, Wavefunction, Inc., Irvine, CA; PM3 force field) in which we deduced the barrier heights to CoNO and $FeO_2$ rotation, using a complete metalloporphyrin, together with all near-neighbor ethyl or phenyl groups, as shown in Figure 11.

Calculations were performed on two four-processor Silicon Graphics/Cray Research (Mountain View, CA) Origin-200 computers in this laboratory, and on SGI Origin-2000 and Power Challenge systems at the National Center for Supercomputing Applications, located in Urbana, IL, using in the latter case up to 16 processors.

## Results and Discussions

**Structural Aspects.** We show in Figures 1−5 the SHELXTL (Bruker) structures of the five new "Fe−$O_2$" analogue model systems: Fe(TPP)(PhNO)(py), Figure 1; Fe(TPP)(NODMA)-(py), Figure 2; Fe(TPP)(PhNO)(1-MeIm), Figure 3; Fe(OEP)-(PhNO)(1-MeIm), Figure 4; and Co(OEP)(NO), Figure 5. Selected structural summaries for all five systems are given in Table 3.

There are several points of interest about the structures of these five systems. The most obvious differences occur in the extent of the porphyrin distortions seen, as illustrated in Figures 6 and 7, where we show the deviations (in $10^{-2}$ Å) of the indicated atoms from the porphyrin least-squares plane. In particular, both of the pyridine-containing TPP complexes, Fe-(TPP)(PhNO)(py) (Figures 1 and 7C) and Fe(TPP)(NODMA)-(py) (Figures 2 and 6A), have major ring distortions, while the two 1-methylimidazole adducts, Fe(TPP)(PhNO)(1-MeIm) (Fig-

(57) Bühl, M. *Chem. Phys. Lett.* **1997**, *267*, 251−257.

(58) Havlin, R.; McMahon, M.; Srinivasan, R.; Le, H.; Oldfield, E. *J. Phys. Chem.* **1997**, *101*, 8908−8913.

(59) Salzmann, R.; McMahon, M.; Godbout, N.; Sanders, L. K.; Wodjelski, M.; Oldfield, E. *J. Am. Chem. Soc.* **1999**, *121*, 3818.

(60) Jameson, G. B.; Rodley, G. A.; Robinson, W. T.; Gagne, R. R.; Reed, C. A.; Collman, J. P. *Inorg. Chem.* **1978**, *17*, 850−857.

(61) Kim, K.; Ibers, J. A. *J. Am. Chem. Soc.* **1991**, *113*, 6077−6081.

**Table 2.** Selected Bond Lengths, Bond Angles, and Torsion Angles Used in Calculations[a]

| | **1**[b] | **2**[b] | **3**[b] mol. 1 | **3**[b] mol. 2 | **4**[b] | **5**[b] | **5**[b,c] | **6**[b] | **7**[b] |
|---|---|---|---|---|---|---|---|---|---|
| $d$(M–N$_{NO}$) | 1.818 | 1.859 | 1.803 | 1.808 | 1.800 | 1.845 | 1.840 | 1.833 | 1.854 |
| $d$(N–O) | 1.252 | 1.251 | 1.258 | 1.270 | 1.254 | 1.152 | 1.167 | 1.15 | 1.195 |
| $d$(M–N$_{Im}$) | 2.113 | 2.096 | 2.094 | 2.091 | 2.029 | | | | |
| $d$(N$_{NO}$–C$_{Ph}$) | 1.468 | 1.436 | 1.454 | 1.448 | 1.444 | | | | |
| $\theta$(M–N–O) | 123.9 | 119.7 | 123.8 | 122.7 | 124.8 | 123.4 | 119.5 | 135.2 | 119.6 |
| $\theta$(O–N–C$_{Ph}$) | 113.0 | 112.3 | 110.1 | 111.7 | 111.3 | | | | |
| $\theta$(N$_{Im}$–M–N$_{NO}$) | 177.4 | 173.7 | 175.4 | 177.8 | 178.7 | | | | |
| $\phi$(N$_{Por}$–M–N$_{base}$–C$_{base}$)[d] | 41.0 | 30.6 | 5.2 | 12.2 | 31.8 | | | | |
| $\phi$(O$_{NO}$–N$_{NO}$–N$_{base}$–C$_{base}$)[e] | 8.5 | 97.2 | 30.5 | 66.2 | 20.2 | | | | |

[a] Bond lengths are in Å, bond angles and torsion angles are in degrees. [b] The structures are as follows: **1**, Fe(TPP)(PhNO)(py); **2**, Fe(TPP)(NODMA)(py); **3**, Fe(OEP)(PhNO)(1-MeIm); **4**, Fe(TPP)(PhNO)(1-MeIm); **5**, Co(OEP)(NO); **6**, Co(TPP)(NO); **7**, Co(Tp-OMePP)(NO). From ref 17. [c] G94/DFT B3LYP partial geometry optimization (see Text for details). [d] This angle gives the orientation of the base (imidazole or pyridine) with respect to the N–Fe–N angle in the porphyrin ring. [e] This angle gives the orientation of the NO ligand with respect to the base (imidazole or pyridine).
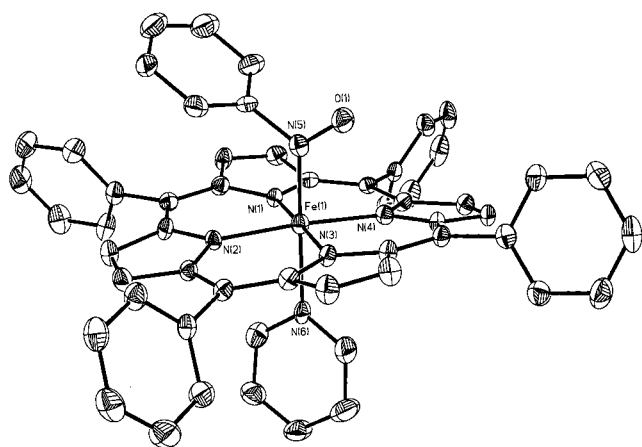


**Figure 1.** X-ray structure of Fe(5,10,15,20-tetraphenylporphyrinate)-(nitrosobenzene)(pyridine). SHELXTL (Bruker, 1998) representation showing 35% probability ellipsoids for non-H atoms. H atoms were omitted for clarity.
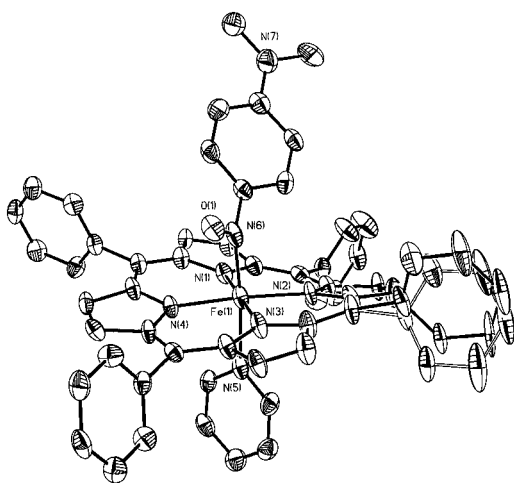


**Figure 2.** X-ray structure of Fe(5,10,15,20-tetraphenylporphyrinate)-(4-nitroso-*N,N*-dimethylaniline)(pyridine). SHELXTL (Bruker, 1998) representation showing 35% probability ellipsoids for non-H atoms. H atoms were omitted for clarity.
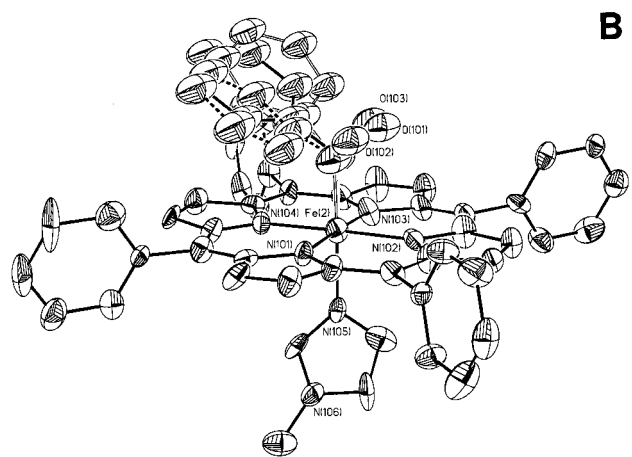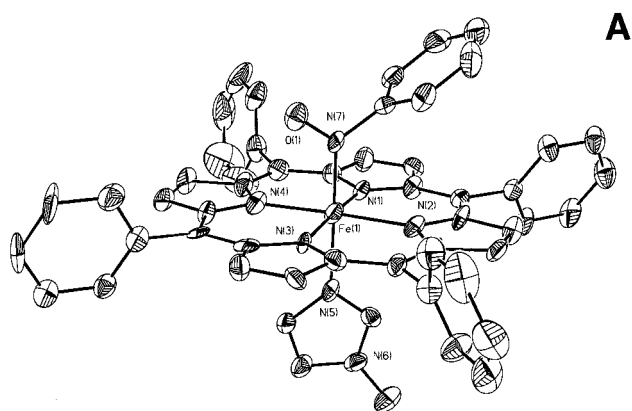


**Figure 3.** X-ray structure of Fe(5,10,15,20-tetraphenylporphyrinate)-(nitrosobenzene)(1-methylimidazole) showing both molecules (A, B) in the unit cell. SHELXTL (Bruker, 1998) representation showing 35% probability ellipsoids for non-H atoms. H atoms were omitted for clarity. Nitrosobenzene disorder is present in B.

ures 3 and 6B,C) and Fe(OEP)(PhNO)(1-MeIm) (Figures 4 and 7A,B), as well as the 5-coordinate OEP species, Co(OEP)(NO) (Figures 5 and 7D), are close to planar. These results are intriguing since they are the opposite of those seen with the M(TPP)(CO)(base) systems discussed earlier,[43] where we found that it was the 1-methylimidazole adducts of M(TPP)(CO) which were ruffled, while the pyridine complexes were planar.[43]

Fortunately, inspection of the structures of the compounds we have synthesized and characterized here, together with our results on the OEP/TPP py/1-MeIm CO adducts, Fe(TPP)-(*i*PrNC)(1-MeIm)[59] and Fe(TPP)(CCl₂),[62] have led to a simple logic-based model for predicting such distortions, as discussed in detail elsewhere.[59] Recapitulating briefly: for the 16 compounds considered,[43,59,62] there are six with highly distorted

(62) We have determined the high-resolution structure of the anhydrous species Fe(TPP)(CCl₂); Ziegler, C.; Salzmann, R.; Suslick, K.; Oldfield, E. unpublished results. The structure of an apparent hydrate was reported by: Mansuy, D.; Lange, M.; Chottard, J. C.; Bartoli, J. F.; Chevrier, B.; Weiss, R. *Angew. Chem., Int. Ed. Engl.* **1978**, *17*, 781–782.
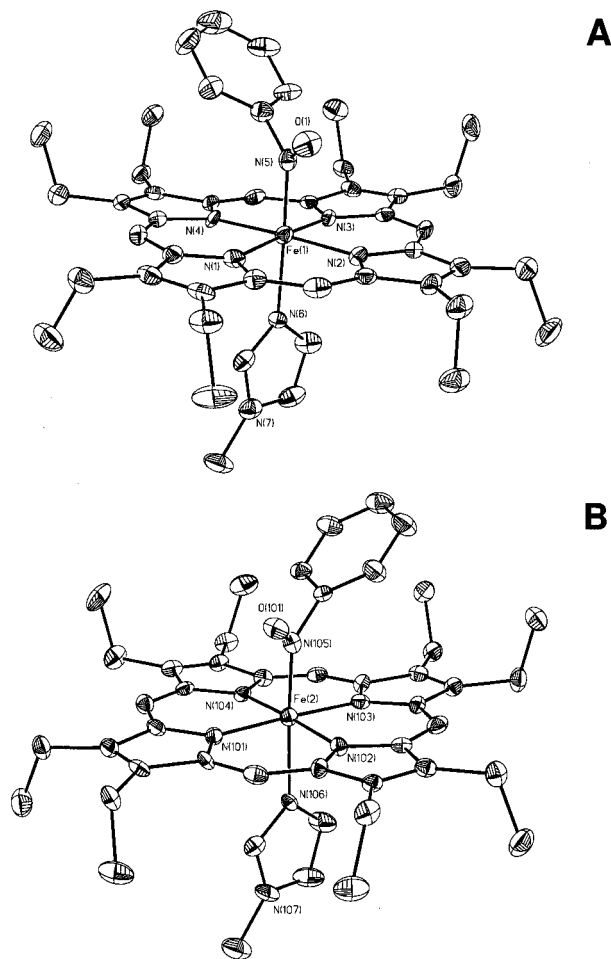
**Figure 4.** X-ray structure of Fe(2,3,7,8,12,13,17,18-octaethylporphyrinate)(nitrosobenzene)(1-methylimidazole) showing both molecules (A, B) in the unit cell. SHELXTL (Bruker, 1998) representation showing 35% probability ellipsoids for non-H atoms. H atoms were omitted for clarity.
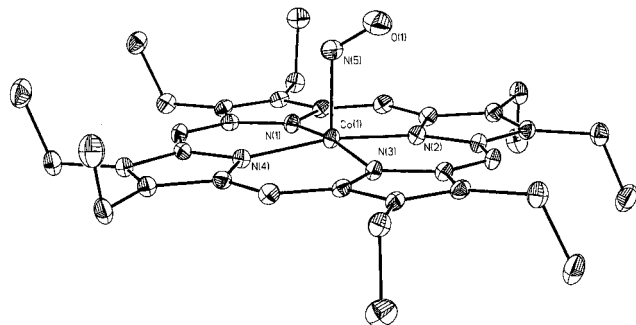


**Figure 5.** X-ray structure of Co(2,3,7,8,12,13,17,18-octaethylporphyrinate)(NO). SHELXTL (Bruker, 1998) representation showing 35% probability ellipsoids for non-H atoms. H atoms were omitted for clarity.

porphyrin rings. These distortions correlate with the presence of porphyrin ring phenyl groups and the presence of one (and only one) of the following large ("distorting") ligands: 1-MeIm, PhNO, NODMA, or CCl$_2$. Thus, Fe(TPP)(PhNO)(py), Figure 1, and Fe(TPP)(NODMA)(py), Figure 2, are distorted, while the other three systems are not, Figures 3−5. As noted before, the presence of two of these "bulky" axial ligands results is a net overall zero distortion.[59] Whether these effects are intra- or intermolecular steric or purely electronic is not certain, but the very large distortions seen with the very bulky NODMA tend to favor steric interactions.

The structures shown in Figures 6 and 7 also indicate that the axial bases in all TPP systems bind with the plane of the axial base oriented at 45° to the N1−N3 axis, i.e., along d$_{xy}$. All four six-coordinate complexes have the metal close to the least-squares plane of the porphyrin, while as expected[16] the Co in Co(OEP)(NO) is above the plane, by about 0.15 Å (Figure 7D). The PhNO and NODMA ligands are also generally oriented with the Fe−N−O plane at 45° to the N1−N3 axes, parallel to the 1-MeIm plane. The same orientation is also seen with the CoNO plane, which unlike previous studies with Co(TPP)NO is not subject to crystallographic or rotational disorder in the OEP case, as discussed below.

Also of interest is the observation that the phenyl rings exhibit a wide range of torsion angles between the nitroso group and the phenyl ring, even though the Fe−N−O angle is relatively constant (at ∼123 ± 3°). In most cases, Table 3, the torsion angle is ∼60−80°, that is, the nitro group is almost perpendicular to the benzene ring, destroying overlap of the two π-systems, presumably due to an otherwise unfavorable hard-core steric repulsive interaction with the π-cloud of the porphyrin ring. However, in the case of the 4-nitroso-*N*,*N*-dimethylaniline, there appears to be a tendency to form the quinonoid-like structure, **2**:
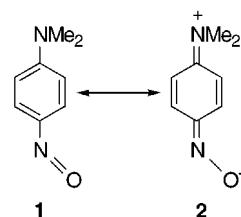


with a C−C−N−O torsion of ∼38° being found for Fe(TPP)-(NODMA)(py). This correlates with an increased tilt of the NODMA group away from the porphyrin plane, with the angle between the phenyl and porphyrin planes increasing from ∼37° to 54°, Table 3. The quinonoid-like structure is also reflected in a slightly shorter C−N bond length (1.457 → 1.437 Å). In the case of Fe(TPP)(PhNO)(1-MeIm), we were unable to obtain a good refinement of one of the two molecules in the unit cell, due to PhNO disorder, so the geometric parameters for this molecule are not included in the above comparisons.

We next briefly compare the main metal−ligand geometric features of these Fe−O$_2$ analogue systems with corresponding values found in oxy-heme proteins and the FeO$_2$ model, oxypicket fence porphyrin.[60] For comparative purposes, we show in Table 4 selected structural parameters for oxy-heme proteins and the model system. As can be seen from Tables 3 and 4, there is generally good agreement in M−A−B bond angles between the Fe•RNO and CoNO model systems and the high-resolution X-ray structure of MbO$_2$, with M−A−B bond angles of ∼120 ± 3° being found in all cases. In the case of the oxy-heme model, the bond angle is slightly larger, but considerable crystallographic disorder was found in this structure, so that these values are likely less accurate. In oxyhemoglobin, the apparent bond angle is 153−159°[2]. While large distortions from the ∼120° observed with the well-characterized systems might be permitted in proteins due to various steric and/or hydrogen bonding/electrostatic field effects, the possibility also exists that the larger protein geometries are more difficult to determine accurately. In the case of CoO$_2$ complexes,[20,21] it is possible that the electronic and geometric structures are indeed different, and do not reflect the situation found with oxy-heme proteins.

**Table 3.** Structural Summary for Fe Porphyrins[a]

| | Fe(TPP)(PhNO)(py) | Fe(TPP)(NODMA)(py) | Fe(TPP)(PhNO)(1-MeIm) | | Fe(OEP)(PhNO)(1-MeIm) | | Co(OEP)(NO) |
| | | | mol.1 | mol. 2[b] | mol. 1 | mol. 2 | |
|---|---|---|---|---|---|---|---|
| M−N(1) | 1.998(3) | 1.972(5) | 1.958(9) | 1.977(8) | 2.012(4) | 1.987(4) | 1.996(2) |
| M−N(2) | 1.990(3) | 2.006(4) | 2.015(8) | 2.011(8) | 1.999(4) | 1.995(4) | 1.980(2) |
| M−N(3) | 1.984(3) | 1.976(5) | 1.973(9) | 2.005(8) | 1.995(4) | 2.003(4) | 1.976(2) |
| M−N(4) | 1.988(3) | 1.970(4) | 1.996(8) | 2.022(8) | 2.003(4) | 2.016(4) | 1.989(2) |
| M−N* | 1.819(3) | 1.859(6) | 1.800(8) | 1.802(3)/1.807(3)/1.812(3) | 1.809(4) | 1.802(4) | 1.844(2) |
| M−N(base) | 2.106(3) | 2.095(5) | 2.029(9) | 2.030(9) | 2.092(4) | 2.094(4) | |
| N*−O | 1.249(4) | 1.252(6) | 1.254(8) | 1.267(3)/1.263(3)/1.260(3) | 1.269(5) | 1.258(4) | 1.152(3) |
| N*−C | 1.472(4) | 1.437(8) | 1.444(9) | 1.453(2)/1.453(2)/1.452(2) | 1.448(6) | 1.454(6) | |
| N(1)−M−N(2) | 88.93(13) | 89.2(2) | 87.8(3) | 90.0(4) | 90.6(2) | 90.1(2) | 89.47(9) |
| N(1)−M−N(3) | 178.08(13) | 178.1(2) | 176.7(4) | 177.6(4) | 176.7(2) | 177.6(2) | 170.98(8) |
| N(1)−M−N(4) | 90.35(12) | 90.1(2) | 92.2(4) | 89.3(4) | 89.3(2) | 90.0(2) | 89.35(8) |
| N(2)−M−N(3) | 90.87(12) | 90.3(2) | 91.8(3) | 89.0(4) | 89.9(2) | 89.9(2) | 90.14(8) |
| N(2)−M−N(4) | 175.14(13) | 174.9(2) | 178.0(4) | 178.7(4) | 177.3(2) | 176.6(2) | 170.06(8) |
| N(3)−M−N(4) | 89.68(12) | 90.3(2) | 88.1(4) | 91.6(4) | 90.0(2) | 89.8(2) | 89.48(8) |
| N*−M−N(1) | 92.41(13) | 91.8(2) | 91.6(4) | 96.5(5)/87.8(6)/89.1(7) | 90.0(2) | 91.3(2) | 95.45(9) |
| N*−M−N(2) | 93.82(13) | 98.2(2) | 91.2(3) | 92.1(3)/91.3(5)/89.4(8) | 91.1(2) | 87.7(2) | 94.60(9) |
| N*−M−N(3) | 89.50(13) | 90.1(2) | 91.6(4) | 85.7(5)/94.3(6)/93.1(7) | 93.3(2) | 91.1(2) | 93.57(9) |
| N*−M−N(4) | 91.02(13) | 86.9(2) | 90.8(3) | 89.1(4)/89.9.5(9)/91.7(8) | 91.6(2) | 95.6(2) | 95.34(9) |
| N*−M−N(base) | 177.24(14) | 173.7(2) | 178.7(3) | 175.4(5)/175.8(6)/176.5(9) | 177.8(2) | 175.4(2) | |
| M−N*−O | 123.9(3) | 119.8(5) | 124.8(7) | 122.8(3)/123.7(3)/124.4(3) | 122.8(3) | 123.8(3) | 123.4(2) |
| M−N*−C | 122.9(3) | 127.0(4) | 123.8(6) | 123.8(3)/124.2(3)/124.3(3) | 122.8(3) | 123.8(3) | |
| O−N*−C | 113.2(3) | 112.3(6) | 111.2(8) | 109.3(3)/110.6(3)/110.8(3) | 111.7(4) | 110.1(3) | |
| torsion amplitude of TPP-phenyl rings | 17°, 23°, 25°, 28° | 12°(20°), 17°, 18°, 18° | 21°, 13°, 8°, 18° | 4°, 2°, 13°, 11° | | | |
| angle between N(base) ring and the porphyrin plane | 100° | 87° | 83° | 84° | 90° | 89° | |
| angle between (*N*-phenyl) plane and the porphyrin plane | 37° | 54° | 37° | 35°/41°/35° | 39° | 39° | |
| angle between (*N*-phenyl) plane and the N−O axis | 24° | 41° | 81° | 42°/21°/39° | 66° | 59° | |

[a] Abbreviations used: M, metal center Fe or Co as appropriate; N*, nitrosyl nitrogen of PhNO or NODMA. [b] Multiple entries exist for values associated with the disordered PhNO group.
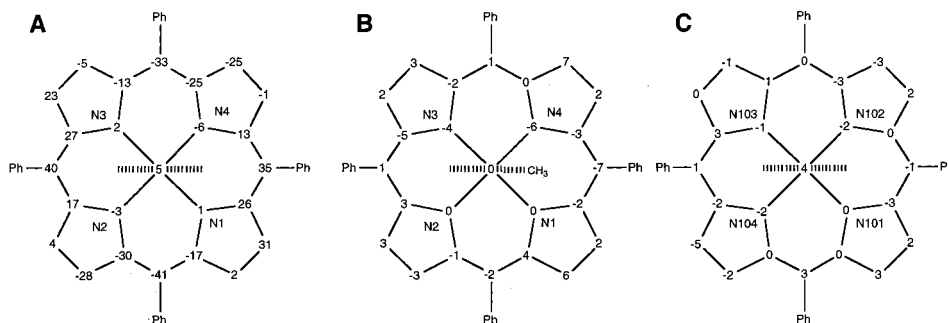


**Figure 6.** Schematic illustration showing atom displacements from the porphyrin least-squares plane (in units of $10^{-2}$ Å) for (A) Fe(TPP)(NODMA)-(py) and (B, C) Fe(TPP)(PhNO)(1-MeIm).

In addition, of course, basic differences in atomic radii, coordination number, and porphyrin substitutions can be expected to lead to small but real differences in observed bond lengths. It is of considerable interest, however, that the observed basic geometry of a ~120° ± 3° M−A−B bond angle is preserved between all three diamagnetic model systems, given the wide variety of metal and ligand types involved.

Given these similarities, it is therefore of interest to next begin to investigate the spectroscopic properties of each of the three different types of model system, using quantum chemical methods to help interpret the results. Such an approach has been used previously by us to investigate the NMR, IR, and Mössbauer spectra of CO bound to metalloporphyrins and metalloproteins, where we concluded that CO binds in a close-to-linear and untilted fashion in both proteins and model systems,[49,50,63] and that electrostatic fields control the differences in IR frequencies seen experimentally with different proteins. Here, we investigate first the Fe•RNO and CoNO metallocycles,

to see to what extent the calculations reproduce the experimental spectroscopic observables in systems having relatively well-defined structures. Then, we consider the FeO₂ system in both metalloporphyrins and in metalloproteins, focusing in particular on the use of $^{57}$Fe Mössbauer spectroscopy as a probe of local structure and bonding. And finally, we use the results of our DFT calculations on the PhNO, O₂, and CO-containing metalloporphyrins to deduce the charge densities, $\rho(\mathbf{r})$, and the molecular electrostatic potentials, $\Phi(\mathbf{r})$, which give useful insights into possible hydrogen bonding interactions in proteins.

**Solid-State NMR and Quantum Chemical Study of Fe•RNO and CoNO Metalloporphyrins.** We have obtained the $^{15}$N and $^{17}$O solid-state (and $^{17}$O solution state) MAS NMR spectra of several $^{15}$N- and $^{17}$O-labeled Fe−O₂ analogue metalloporphyrins, including Fe(TPP)([$^{15}$N]-PhNO)(py), Fe-
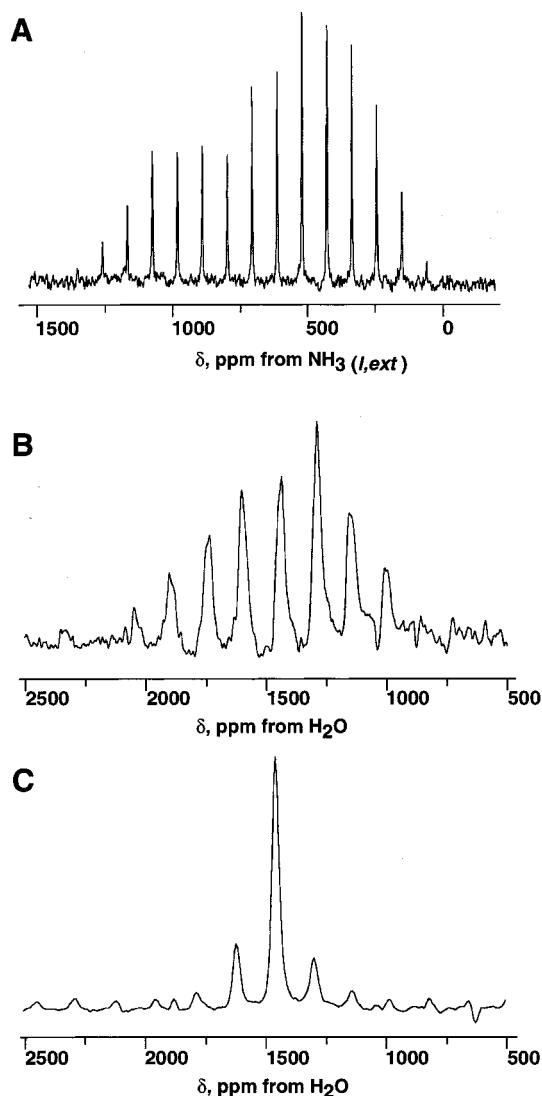
(63) McMahon, M. T.; deDios, A. C.; Godbout, N.; Salzmann, R.; Laws, D. D.; Le, H.; Havlin, R. H.; Oldfield, E. *J. Am. Chem. Soc.* **1998**, *120*, 4784−4797.

**Table 4.** Selected Structural Parameters of Oxy-Heme Proteins and Model Systems[a]

| PDB file no.[b] | $d(O-O)$ | $d(Fe-O)$ | $d(Fe-N_{Im})$ | $\theta(Fe-O-O)$ | $\theta(O-O-Fe-N_{Por})$ | $\phi(N_{Por}-Fe-N_{Im}-C_{Im})$ Im orient. wrt N−Fe−N | $\phi(O-O-N_{Im}-C_{Im})$ O$_2$ orient. wrt Im |
|---|---|---|---|---|---|---|---|
| 1HHO ($\beta$ subunit) | 1.24(2) | 1.87(13) | 2.07(9) | 159.0(12) | 40 | 24.8 | 68.4 |
| 1HHO ($\alpha$ subunit) | 1.22(1) | 1.66(8) | 1.94(9) | 153.0(7) | 19 | 12.0 | 8.2 |
| 1MBO | 1.22(6) | 1.83(6) | 2.07(6) | 115(5) | 20 | 2.4 | 23.2 |
| 2MGM | 1.22 | 1.94 | 2.19 | 118.2 | 41 | 1.3 | 43.6 |
| 2SPN | 1.29 | 1.93 | 2.30 | 120.3 | 7 | 2.6 | 6.7 |
| picket[c] | 1.17(4) | 1.75(2) | 2.07(2) | 129(2) | 48.0 | 20.5 | 117.1 |

[a] Bond lengths are in Å, bond angles and dihedral angles are in deg. Available error values are shown in parentheses. [b] The structures given typically refer to Brookhaven Protein Data Bank file numbers: 1HHO: B. Shaanan, hemoglobin A (oxy), human (*Homo sapiens*), 2.1 Å resolution (1984); 1MBO: S. E. V. Phillips, myoglobin (oxy, pH 8.4), sperm whale (*Physeter catodon*), 1.6 Å resolution (1983); 2MGM: M. L. Quillin, R. M. Arduini, G. N. Phillips, Jr., myoglobin (oxy) mutant with initiator Met and Asp 12 replaced by Asn (Met, D122N), synthetic gene for sperm whale myoglobin expressed in *Escherichia coli*, 1.9 Å resolution (1994); 2SPN, M. L. Quillin, R. M. Arduini, G. N. Phillips, Jr., myoglobin (oxy) mutant with initiator Met, Leu 29 replaced by Phe, and Asp 122 replaced by Asn (Met, L29F, D122N), sperm whale myoglobin expressed in *E. coli*, 1.7 Å resolution (1994). [c] Reference 60.
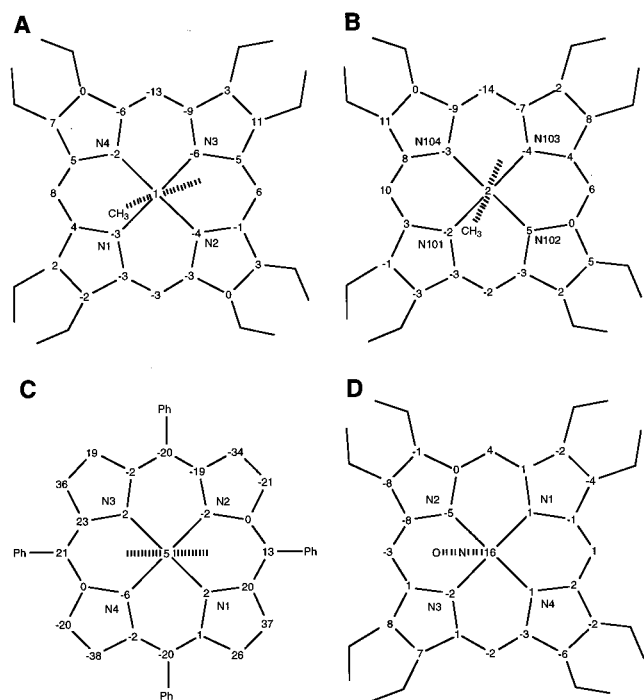


**Figure 7.** Schematic illustration showing atom displacements from the porphyrin least-squares plane (in units of $10^{-2}$ Å) for: (A, B) Fe-(OEP)(PhNO)(1-MeIm), (C) Fe(TPP)(PhNO)(py) and D, Co(OEP)NO.



**Figure 8.** Representative NMR spectra of metalloporphyrins investigated. (A) 8.45 T $^{15}$N MAS NMR spectrum of Fe(TPP)(Ph$^{15}$NO)(py) at 298 K; (B) 11.7 T $^{17}$O MAS NMR spectrum of Co(OEP)(N$^{17}$O) at 373 K; and (C) 11.7 T $^{17}$O MAS NMR spectrum of Co(TPP)(N$^{17}$O) at 298 K.

(TPP)([nitroso-$^{15}$N]-NODMA)(py), Fe(TPP)([$^{15}$N]-PhNO)(1-MeIm), Co(OEP)($^{15}$NO), Co(OEP)(N$^{17}$O), and Co(TPP)(N$^{17}$O). These compounds all have quite well characterized structures and offer the opportunity to deduce shielding information about both the directly attached nitroso nitrogens (in Co and Fe systems) and the terminal oxygen atom in the Co•NO system. We report first the solid-state NMR spectra of these systems, and show that the DFT calculations give relatively good shielding predictions. We then consider in the next section our $^{57}$Fe Mössbauer results, and the corresponding EFG (Mössbauer $\Delta E_Q$) calculations. Since the shielding tensors are response properties, they are often more difficult to evaluate than are electric field gradient tensors, which depend primarily on the description of the ground rather than ground-and-excited states of the molecule. Success in evaluating both shift and EFG tensors (see below) gives increased confidence in the reliability of the theoretical methods to predict these observables, as well as others, such as the charge density and the electrostatic

potential,[37−39] which can then begin to be used to describe the details of, e.g., hydrogen bonding, in these and related systems.

We show in Figure 8 typical $^{15}$N and $^{17}$O NMR spectra: the $^{15}$N MAS NMR spectrum of Fe(TPP)([$^{15}$N]-PhNO)(py) (Figure

*O₂-Heme Analogue Studies*

*J. Am. Chem. Soc., Vol. 121, No. 16, 1999* 3837

**Table 5.** Comparison between Experimental and Computed Chemical Shifts and Shift Tensor Elements for Fe−O$_2$ Analogue Metalloporphyrins[a]

| system | | | $\delta_i$(ppm) | $\delta_{11}$ (ppm) | $\delta_{22}$(ppm) | $\delta_{33}$ (ppm) | $\lvert\delta_{33} - \delta_{11}\rvert$ (ppm) |
|---|---|---|---|---|---|---|---|
| Fe: Fe(TPP)(Ph$^{15}$NO)(1-MeIm) | | expt | 605 | 1178 | 464 | 173 | 1005 |
| Fe(P)(Ph$^{15}$NO)(1-MeIm) | | calc | 628 | 1220 | 486 | 179 | 1041 |
| Fe(TPP)(Ph$^{15}$NO)(py) | | expt | 607 | 1265 | 469 | 87 | 1178 |
| Fe(P)(Ph$^{15}$NO)(py) | | calc | 644 | 1256 | 490 | 186 | 1070 |
| Fe(TPP)($^{15}$NO−NODMA)(py) | | expt | 607 | 1281 | 456 | 82 | 1199 |
| Fe(P)($^{15}$NO−NODMA)(py) | | calc | 603 | 1170 | 472 | 168 | 1002 |
| Fe(OEP)(Ph$^{15}$NO)(1-MeIm) | | expt | 593 | 1247 | 448 | 84 | 1163 |
| Fe(P)(Ph$^{15}$NO)(1-MeIm) | site 1 | calc | 643 | 1246 | 500 | 182 | 1064 |
| | site 2 | | 623 | 1202 | 486 | 182 | 1020 |
| Co: Co(OEP)($^{15}$NO) | | expt | 1155 | 2070 | 829 | 566 | 1504 |
| Co(P)($^{15}$NO) | | calc | 908 | 1901 | 561 | 263 | 1638 |
| Co(OEP)(N$^{17}$O) | 298 K | expt | 1430 | 2674 | 959 | 656 | 2018 |
| | 343 K | | 1445 | 2288 | 1247 | 801 | 1487 |
| | 373 K | | 1441 | 1959 | 1376 | 987 | 972 |
| | 393 K | | 1445 | 1868 | 1475 | 993 | 875 |
| Co(P)(N$^{17}$O) | | calc | 1232 | 2747 | 779 | 170 | 2577 |
| Co(TPP)(N$^{17}$O) | 298 K | expt | 1458 | 1670 | 1505 | 1200 | 470 |

[a] The theoretical chemical shieldings ($\sigma$) were calculated as described in the text and were then converted to theoretical chemical shifts ("calc" in the Table) by using the following absolute shieldings: $^{15}$N, $\delta$($^{15}$N, NH$_3$) ppm = 244.6 − $\sigma$ (ref 74) and for $^{17}$O, $\delta$($^{17}$O, H$_2$O) ppm = 306.7 − $\sigma$ (ref 75).

8A), the $^{17}$O MAS NMR spectrum of Co(OEP)(N$^{17}$O) (Figure 8B), and the $^{17}$O MAS NMR spectrum of Co(TPP)(N$^{17}$O) (Figure 8C). From such spectra, we obtained the principal components of the $^{15}$N and $^{17}$O chemical shift tensors, and/or the isotropic chemical shifts, shown in Table 5. We then evaluated the individual components of the $^{15}$N and $^{17}$O shielding tensors and the corresponding isotropic shifts. These results are also presented in Table 5, and a graphical comparison between the experimental and theoretical shift tensor results is given in Figure 9. There is clearly a good overall correlation between theory and experiment, although the errors in absolute shielding are rather more pronounced for these axial ligands (NO and RNO) than are seen with the CO and RNC systems,[43,59] presumably due to the small n → $\pi$* separation in the NO group, and the large overall paramagnetic shifts. Typical shielding tensor orientations for the Fe•RNO and Co•NO systems are shown in Figure 10. As can be seen from Figures 10A and 10B, the orientations of the two tensors are in general similar with the most deshielded element, $\sigma_{11}$, oriented along or close to the N=O bond axis, while the most shielded element, $\sigma_{33}$, is oriented perpendicular to the M−N−O plane. Having $\sigma_{11}(\delta_{11})$ oriented close to the N−O bond axis and $\sigma_{33}(\delta_{33})$ more or less perpendicular to the R−N−O (or M−N−O) plane is the orientation seen in many other nitrosocompounds, as discussed previously.[64]

Now, to fully describe the observed spectra, we must consider the effects that molecular motion might have on the spectroscopic observables—a topic of great debate for many years in the context of Fe−O$_2$ interactions in heme proteins and model systems, as described below. We find a major temperature dependence of the $^{17}$O CSA in Co(OEP)(NO), Table 5. At 23 °C, the tensor is close to axially symmetric, with an overall span of ~2000 ppm, while at 120 °C (shortly before the onset of NO loss) the tensor has narrowed considerably, to a span of ~900 ppm, due most likely to fast axial rotation of the Co−NO group, as found also with oxypicket fence porphyrin.[11,14] The tensor is, however, still considerably broader than the ~470 ppm observed with Co(TPP)(NO) at 23 °C, Table 5, possibly due to not attaining its fast motion limit. This is consistent with the previous $^{15}$N NMR observations of Groombridge et al.[65] on

Co(TPP)($^{15}$NO), in which they observed fast axial motion of the Co−NO fragment at 298 K, but an essentially rigid lattice tensor at 200 K, with a phase transition at 206.7 K.[65]

In the case of Co(OEP)(NO), the $^{17}$O NMR results indicate a major increase in the barrier to axial rotation from that seen in Co(TPP)(NO). There is essentially free rotation at room temperature with Co(TPP)(NO), but hindered rotation or essentially no motion at room temperature in the case of Co(OEP)-(NO), as judged by $^{17}$O NMR, and via crystallography. These results are linked to strong steric interactions between the bent NO group and the ethyl groups in OEP, while in the TPP analogue the phenyl groups act more as lattice spacers. This effect can be well reproduced by carrying out a molecular mechanics (PM3; Spartan) study of the rotational barrier using single Co(TPP)(NO) or Co(OEP)(NO) molecules together with additional local ethyl or phenyl groups from neighboring molecules, as shown schematically in Figures 11A,B. In the case of TPP, Figure 11, the barrier to rotation is very small (1.6 kcal) and has 4-fold symmetry, making hopping from one state to another quite facile at room temperature (and thereby making X-ray refinements very difficult). In contrast, in the case of Co(OEP)(NO), there are major steric interactions with neighboring ethyl groups, with a barrier height of ~18 kcal mol$^{-1}$, Figure 11C, although of course in reality this will be reduced due to ethyl librations. The presence of such fast axial rotation enables an estimate of the Co−N−O bond angle from the NMR data, as reported previously with the Fe−O−O fragment in oxypicketfence porphyrin,[11] and in Co(TPP)(NO).[65] Using a value of −388 ppm ($^1$/$_2$(1670 + 1505) − 1200) as an estimate of the motionally averaged tensor span from the shielding calculations, and $\Delta\delta$ = 2747 − $^1$/$_2$(779 − 170) = 2442 ppm as the theoretical rigid lattice limit, we obtain from $\bar{\Delta}\delta = {}^1$/$_2$(3 cos$^2$ $\theta$ − 1)$\Delta\delta$ (ref 11) a value for $\theta$, the Co−N−O bond angle, of about 118.5°. This value is almost identical to the 119.5° we obtain by using a DFT quantum chemical geometry optimization (Table 2), and the recent value of 119.6° obtained crystallographically by Richter-Addo for Co(T(p-OMe)PP)(NO).[17] All of these values are somewhat smaller than the ~127−135° range reported previously, for related compounds.[16,65] In any event, a Co−N−O bond angle of close to 120° now seems to be most general, since neither of the most

(64) Salzmann, R.; Wojdelski, M.; McMahon, M.; Havlin, R. H.; Oldfield, E. *J. Am. Chem. Soc.* **1998**, *120*, 1349−1356.

(65) Groombridge, C. J.; Larkworthy, L. F.; Mason, J. *Inorg. Chem.* **1993**, *32*, 379−380.
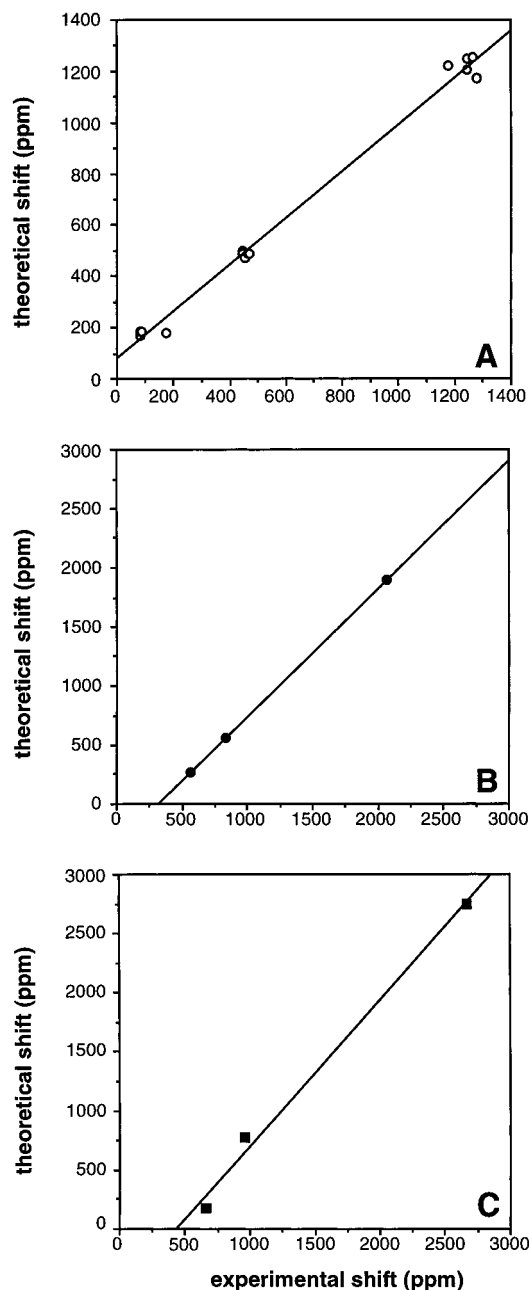
**Figure 9.** Graphs showing correlations between experimental and theoretical chemical shifts for $^{15}N$, $^{17}O$-labeled metalloporphyrins: (A) R$^{15}$NO, slope = 0.910, $R^2$ = 0.993; (B) Co$^{15}$NO, slope = 1.09, $R^2$ = 1.00; and (C) CoN$^{17}$O, slope = 1.233, $R^2$ = 0.992. From Table 5.

recent crystal structures were plagued by crystallographic disorder. The fact that the CoNO bond angle is also found to be essentially 120° by using quantum chemical methods (Table 2) gives additional confidence in the use of such methods in the structure refinement of $FeO_2$ and $Fe-O_2$ analogue metalloporphyrins and metalloproteins.

**The Iron-57 Mössbauer Problem.** We next investigate the question of the $^{57}$Fe Mössbauer spectroscopy of $FeO_2$ and $Fe-O_2$ analogue metalloporphyrins and metalloproteins. Here, there have been major questions as to the geometry of $Fe-O_2$ bonding (bent versus symmetric, the degree of bend of the $Fe-O-O$ unit), as well as many discussions of electronic structure (see, e.g., refs 66–70). While quantum chemical methods have been

applied in the past to analyze Mössbauer spectra, only more recently have the results of the calculations become "robust"— that is they give the correct results for a broad range of bonding situations without adjustable parameters,[49,71] in a reliable way. Indeed, as clearly shown by Case and co-workers, the results of early (e.g., Xα, EHT, PPP) calculations gave all sorts of EFG and orbital energy predictions—a situation that for most systems of interest has now been rectified by use of modern DFT methods.[49,71]

Experimentally, $^{57}$Fe Mössbauer spectroscopy is a potentially powerful probe of the $^{57}$Fe center, and thereby of $Fe-O_2$ structure and bonding, and several studies on model systems, such as oxypicket fence porphyrins, as well as on myoglobin and hemoglobin, have been reported.[13–15] The Mössbauer results on a single crystal of oxymyoglobin indicate that the principal component of the electric field gradient tensor at Fe, $V_{zz}$, defined such that

$$|V_{zz}| \geq |V_{yy}| \geq |V_{xx}| \text{ and } V_{xx} + V_{yy} + V_{zz} = 0$$

is oriented in the plane of the porphyrin,[13] at least at low temperatures. In addition, the magnitude of the observed Mössbauer quadrupole splitting, $\Delta E_Q$, defined as:

$$\Delta E_Q = \frac{1}{2}eQV_{zz}\left(1 + \frac{\eta^2}{3}\right)^{1/2}$$

where $Q$ is the quadrupole moment of the $I^* = {}^3/_2$ excited state and $\eta$ is the asymmetry parameter of the electric field gradient:

$$\eta = \frac{V_{xx} - V_{yy}}{V_{zz}}$$

is temperature dependent. In oxypicket fence porphyrin, $\Delta E_Q$ varies from about $-2.1$ mm s$^{-1}$ at 4.2 K[14] to about 1.3 mm s$^{-1}$ (unsigned) at room temperature, while in oxymyoglobin, $\Delta E_Q$ is about $-2.3$ mm s$^{-1}$ at 4.2 K and increases to $\sim|1.6|$ mm s$^{-1}$ at 260 K.[15] A variety of models have been used to explain these results, as discussed for example by Debrunner.[15] In one model, the $MbO_2$ data have been rationalized in terms of a harmonic model of bond angle and bond distance oscillations,[15,72] while Spartalian et al.[14] have proposed a 2-site jump model for oxypicket fence porphyrin, in which there are two substates, having $QV_{ii}$ of $-4.18$, 1.60, 2.57 and $-1.78$, 0.18, and 1.60 mm s$^{-1}$,[14] while in a third model, iterative extended Hückel theory has been used to support a rotational diffusion model.[12]

Here, we first investigate the Fe•RNO adducts via Mössbauer spectroscopy and quantum chemistry, to test the ability of DFT methods to predict the observable $\Delta E_Q$ values in these $Fe-O_2$ analogue systems whose structures are accurately known. Then, we apply the same quantum chemical methods to the problem of the $^{57}$Fe Mössbauer spectroscopy of oxypicket fence por-

(66) Pauling, L. *Nature* **1964**, *203*, 182–183. Weiss, J. J. *Nature* **1964**, *203*, 183.

(67) Olafson, B. D.; Goddard, W. A., III *Proc. Natl. Acad. Sci. U.S.A.* **1977**, *74*, 1315–1319.

(68) Case, D. A.; Huynh, B. H.; Karplus, M. *J. Am. Chem. Soc.* **1979**, *101*, 4433–4453.

(69) Newton, J. E.; Hall, M. B. *Inorg. Chem.* **1984**, *23*, 4627–4632.

(70) Dedieu, A.; Rohmer, M.-M.; Veillard, H.; Veillard, A. *Nouv. J. Chim.* **1979**, *3*, 653–667.

(71) Grodzicki, M.; Flint, H.; Winkler, H.; Walker, F. A.; Trautwein, A. X. *J. Phys. Chem.* **1997**, *101*, 4202–4207.

(72) Wise, W. W.; Debrunner, P. G. *Bull. Am. Phys. Soc.* **1984**, *29*, 365.

(73) W. Arnold, N. Godbout, and E. Oldfield, unpublished results.

(74) Jameson, C. J.; Jameson, A. K.; Oppusunggu, D.; Willie, S.; Burrell, M.; Mason, J. *J. Chem. Phys.* **1981**, *74*, 81–88.

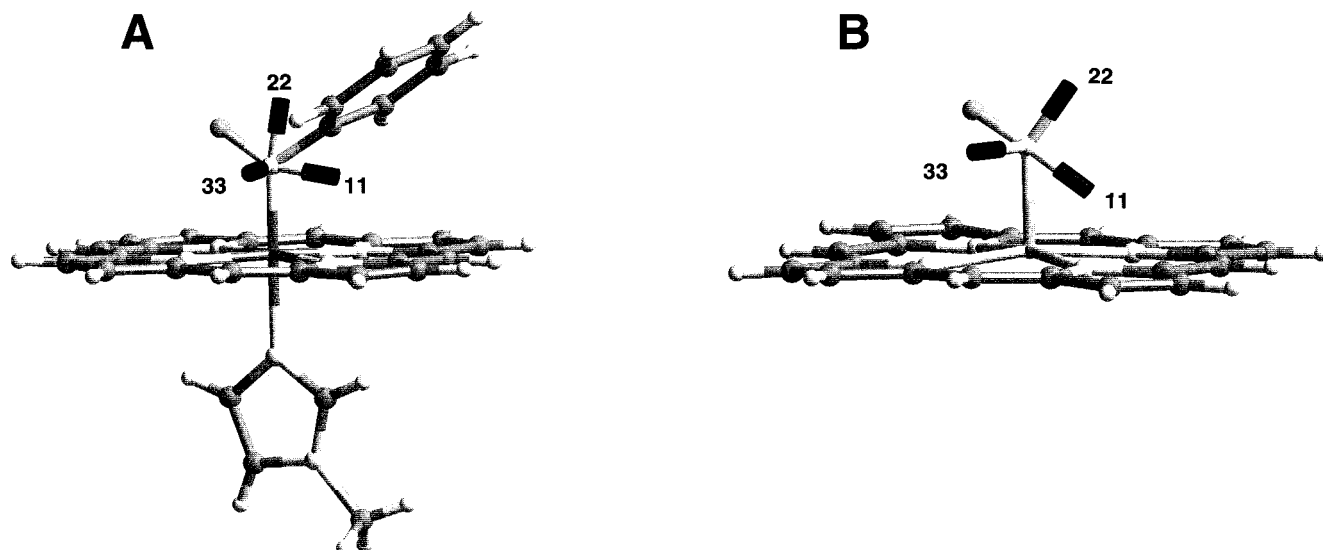(75) Wasylishen, R. E.; Mooibroek, S.; Macdonald, J. B. *J. Chem. Phys.* **1984**, *81*, 1057–1059.

**Figure 10.** Orientations of the principal components of the ¹⁵N shielding tensors for two metalloporphyrins: (A) Fe(TPP)(Ph¹⁵NO)(1-MeIm) and (B) Co(OEP)(¹⁵NO).
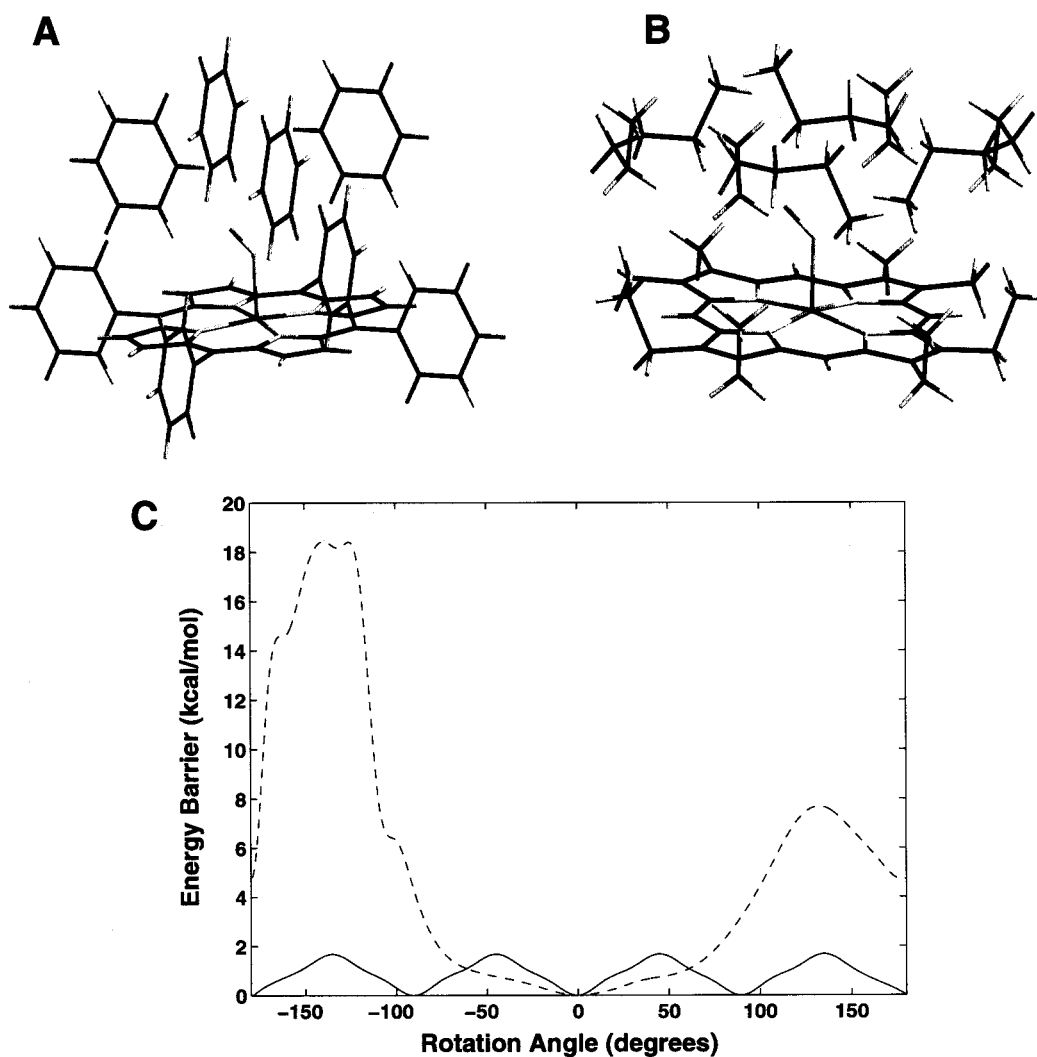


**Figure 11.** Barriers to NO ligand rotation in CoNO porphyrins. (A, B) Co(TPP)(NO) and Co(OEP)(NO) molecules and lattice fragments used to evaluate the barriers to rotation and (C) rotational barriers. Co(TPP)(NO) is shown as a solid line; Co(OEP)(NO) is shown as a dashed line. The barriers were evaluated by using molecular mechanics (Spartan 4.1) allowing only Co−NO rotation.

phyrin and oxymyoglobin, testing some of the ideas put forth previously, which then leads to a final investigation of electro-statics in these and related systems.

We show in Figure 12A a representative ⁵⁷Fe Mössbauer spectrum of Fe(TPP)(PhNO)(1-MeIm) at 298 K, together with a spectral simulation, in addition to ⁵⁷Fe Mössbauer spectra of
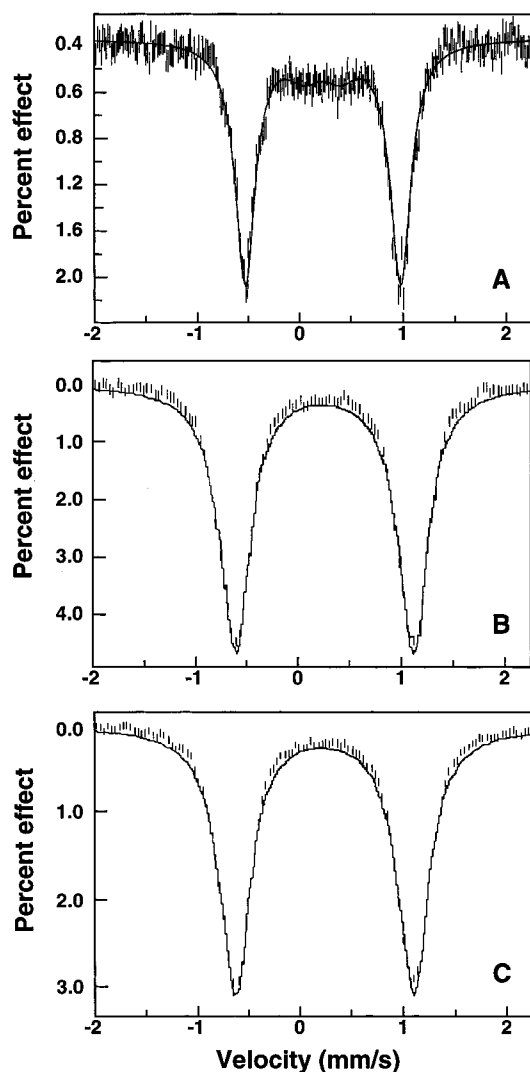
**Figure 12.** Representative $^{57}Fe$ Mössbauer spectra: (A) Fe(TPP)-(NODMA)(py), at 298 K; (B) [$^{57}Fe$] Mb•PhNO at 50 K and (C) [$^{57}Fe$]-Mb•PhNO at 200 K.

[$^{57}Fe$]Mb•PhNO at 50 and 200 K, Figures 12B and 12C, respectively. The observed quadrupole splittings for both the protein and model compounds (Table 6) are quite large and are similar in magnitude to those observed previously for Fe(TPP)-(iPrNO)(nPrNH$_2$) by Mansuy et al.[18,19] in their pioneering studies of nitrosoalkane-containing metalloporphyrins, in which the sign of $\Delta E_Q$ was determined to be negative. We then carried out $^{57}Fe$ EFG calculations using DFT (G94/DFT/B3LYP/Fe Wachters'/6-311++G(2d)/6-31G*/3-21G*), with the results shown in Table 6. As can be seen from Table 6, the $\Delta E_Q$ values computed from the known crystal structures vary from −0.98 to −1.4 mm s$^{-1}$, to be compared with the experimental range of from −1.3 to −1.5 mm s$^{-1}$, about a 0.2 mm s$^{-1}$ error— about the same error range as that reported previously for 14 organometallic and metalloporphyrin model compounds.[49] Also of interest is the observation that the orientation of the principal component of the EFG tensor, $V_{zz}$, is in the porphyrin plane, Figure 13, just as it is with oxymyoglobin,[13] a result that might be anticipated based on the isoelectronic nature of Fe•O$_2$ and Fe•RNO (Fe•HNO) systems. This gives strong support for the use of DFT calculations to predict the EFGs in metalloporphyrins, and indeed in work described elsewhere we have found good accord for $\Delta E_Q$ for Fe(TPP)(CO)(1-MeIm), Fe(TPP)(CO)-(py), Fe(TPP)(py)$_2$, Fe(TMP)(1-MeIm)$_2$, Fe(OEP)(PMe$_3$)$_2$, and

a cytochrome *c* model,[49] as have Walker et al. for the PMe$_3$ and TMP adducts noted above.[71] We therefore next consider the FeO$_2$ systems, oxypicket fence porphyrin and oxymyoglobin. In these O$_2$ containing systems there is more uncertainty in the geometries to be used, since oxypicket fence porphyrin has crystallographic disorder,[60] and in proteins the FeO$_2$ geometries and porphyrin ruffles are less certain, although disorder is clearly less of a problem than with the picket fence system.[42]

We first carried out an exploratory series of calculations using both a planar (C$_2$-cap) and a less planar (picket fence) porphyrin geometry, using $d(Fe-O) = 1.75$ Å, $d(O-O) = 1.24$ Å, and $\angle Fe-O-O = 131°$,[60] together with several basis sets, functionals, and FeO$_2$/1-MeIm/porphyrin geometries. The results of these initial calculations are shown in Table 6 and indicate $\Delta E_Q$ values ranging from −1.7 to −2.4 mm s$^{-1}$, $V_{zz}$ is in the porphyrin plane (Figure 13), and $\eta$ is small (∼0.1−0.3). This is all in good accord with experiment, and most importantly, the calculations are essentially identical in form to previous successful EFG ($\Delta E_Q$) calculations for other (CO, RNC, cytochrome *c*, RNO, PMe$_3$) metalloporphyrin systems, indicating reliability. The results shown in Table 6 also indicate that there is a significant effect of porphyrin geometry on the computed $\Delta E_Q$ values, although the effects of rotating the O$_2$ ligand by 90°, 180°, and 270° are quite small (only 0.07 mm s$^{-1}$). On the basis of these results, there seems to be little support for the existence of a second site having $\Delta E_Q \sim -0.9$ mm s$^{-1}$ as being the origin of the temperature-dependent Mössbauer results.[14] We then extended our calculations to cover the six major imidazole/FeO$_2$/porphyrin relative orientations shown schematically in Figure 14, since these relative orientations might be significant in causing EFG changes at Fe. We also carried out geometry optimizations of the FeO$_2$ fragment ($d(Fe-$O), $d(O-O)$, $\angle Fe-O-O$). The optimized structural parameters are shown in Table 7, together with their relative energies. The results of the unoptimized ($d(Fe-O) = 1.75$ Å, $d(O-O) = 1.24$ Å, $\angle Fe-O-O = 131°$) and optimized EFG calculations are shown in Table 8, for an essentially undistorted metalloporphyrin. These results do show a sizable range in $\Delta E_Q$ (from −1.53 to −2.62 mm s$^{-1}$), but all values are far larger than the tensor required in the early model[14] to describe the temperature dependence of the $^{57}Fe$ Mössbauer $\Delta E_Q$ in picket fence porphyrin.[14] Interestingly, there is only a small change in $\Delta E_Q$ on geometry optimization, Table 8. We then evaluated the $\Delta E_Q$ values for six ruffled porphyrins, Table 8, with results in general accord with those obtained using the planar model, except that the range of $\Delta E_Q$ varied from −1.86 to −2.65 mm s$^{-1}$.

These results demonstrate that DFT methods give both the correct magnitude for $\Delta E_Q$ in oxyheme models, and the correct sign, orientation (Figure 13), and $\eta$ values, but they also point to the difficulty of accurately describing the oxyheme geometry by using just $\Delta E_Q$. On the basis of the latest high-resolution crystal structures of MbO$_2$,[42] it appears that the proximal histidine (our 1-MeIm axial base) is oriented along an N1−N3 vector, thus the models shown in Figures 14D−F would be closest to experiment, with E also being in good agreement with the Fe−O−O orientation seen in two oxymyoglobins, Table 4. The energies of B, C, and E in Figure 14 (Table 7) are also the lowest of the series, which when combined with the X-ray data suggests conformer E as a likely candidate for accurate EFG calculations. The results we obtain are $\Delta E_Q = -1.84, -1.82$, and −2.45 mm s$^{-1}$ for the planar/unoptimized, planar/optimized, and ruffled/unoptimized structures, and at present it is not possible to get more accurate results, although this may be possible in the future by carrying out very large scale geometry

**Table 6.** Computed $^{57}$Fe Electric Field Gradient Tensor Elements and Mössbauer Quadrupole Splittings for RNO, O$_2$-Metalloporphyrins, and Experimental Data for Mb•PhNO

| | electric field gradient (au) | | | $\Delta E_Q$ (mm s$^{-1}$) | |
|---|---|---|---|---|---|
| | $V_{11}$ | $V_{22}$ | $V_{33}$ | calc | expt |
| (PhNO)(1-MeIm)(TPP)Fe[a] | −0.3738 | −0.2216 | 0.5954 | −0.975 | -1.31[b] |
| (PhNO)(py)(TPP)Fe[a] | −0.6162 | −0.1433 | 0.7595 | −1.31 | −1.42[b] |
| (p-Me$_2$NC$_6$H$_4$NO)(py)(TPP)Fe[c] | −0.7498 | 0.0187 | 0.7311 | 1.39 | 1.51[b] |
| PhNO•Mb | | | | | |
|   50 K | | | | | −1.758[b] |
|   100 K | | | | | −1.758[b] |
|   150 K | | | | | −1.752[b] |
|   200 K | | | | | −1.747[b] |
| (O$_2$)(1-MeIm)(TPP)Fe (C$_2$-cap)[d] | −0.8430 | −0.6480 | 1.4911 | −2.42 | |
| (O$_2$)(1-MeIm)(TPP)Fe (C$_2$-cap)[e] | −0.8081 | −0.6392 | 1.4472 | −2.35 | |
| (O$_2$)(1-MeIm)(TPP)Fe (C$_2$-cap) BP86[e,f] | −0.8337 | −0.6223 | 1.4560 | −2.37 | |
| (O$_2$)(1-MeIm)(TPP)Fe (C$_2$-cap) BPW91[g] | −0.8397 | −0.6174 | 1.4527 | −2.36 | |
| (O$_2$)(1-MeIm)(TPP)Fe (picket) xray[e,h] | −0.7128 | −0.3731 | 1.0859 | −1.79 | −2.1, −2.25, −2.31[i] |
| (O$_2$)(1-MeIm)(TPP)Fe (picket) xray+90[d,h,j] | −0.7007 | −0.3471 | 1.0478 | −1.73 | |
| (O$_2$)(1-MeIm)(TPP)Fe (picket) xray+180[d,h,j] | −0.7116 | −0.3720 | 1.0837 | −1.78 | |
| (O$_2$)(1-MeIm)(TPP)Fe (picket) xray+270[d,h,j] | −0.7022 | −0.3442 | 1.0464 | −1.73 | |
| (O$_2$)(1-MeIm)(TPP)Fe (picket) xray $d$(O−O) = 1.24 Å [d,h,k] | −0.7910 | −0.4132 | 1.2043 | −1.98 | |

[a] G94/B3LYP/Fe Wachters/6-311++G(2d) NO and N coordinated to Fe/6-31G* Cα/3-21G* others. [b] This work. [c] G94/B3LYP/Fe Wachters/6-311++G(2d) N coordinated to Fe/6-31G* Cα/3-21G* others. [d] G94/B3LYP/Fe Wachters/6-311++G(2d) O$_2$ and N coordinated to Fe/6-31G* Cα/3-21G* others. [e] G94/B3LYP/Fe Wachters/6-311G(2d) O$_2$ and N coordinated to Fe/6-31G* Cα/3-21G* others. [f] BP86 exchange-correlation functional (ref 23). [g] G94/BPW91 (ref 54)/Fe Wachters/6-311++G(2d) O$_2$/6-31G* others. [h] X-ray structure from ref 60. [i] Experimental data from ref 14 and ref 15. [j] X-ray + angle value means the Fe−O−O fragment was rotated with respect to the porphyrin normal by the amount indicated. [k] $d$(O−O) was set at 1.24 Å.
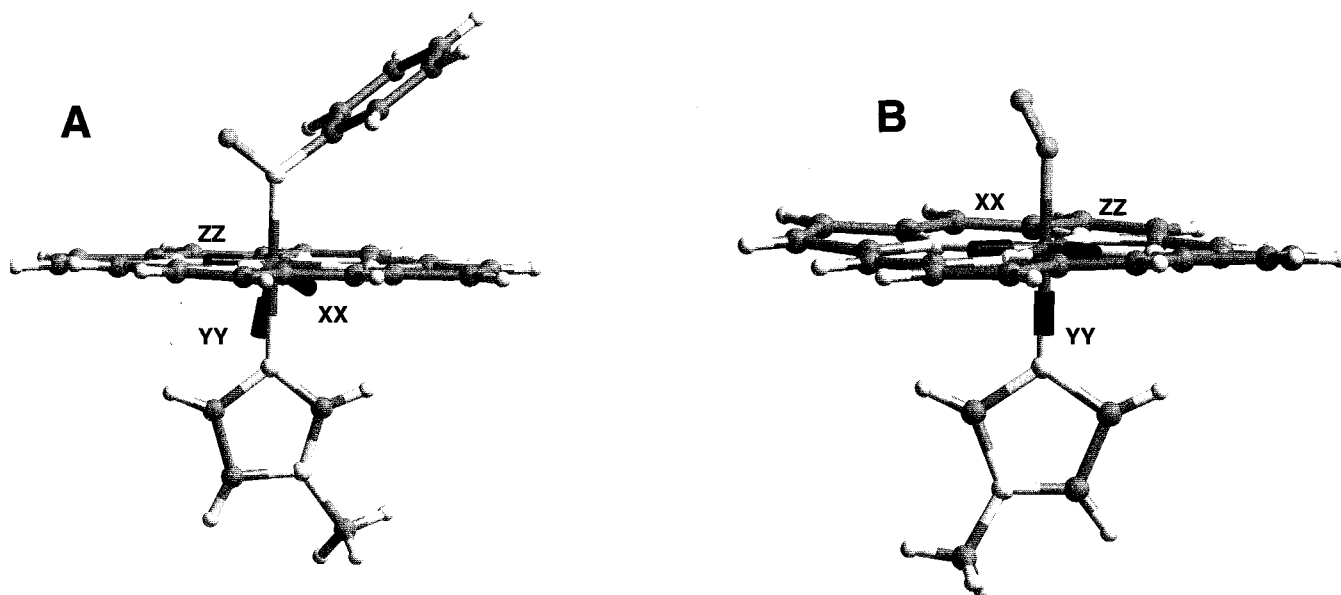


**Figure 13.** Orientations of the principal components of the electric field gradient tensor for $^{57}$Fe in RNO, O$_2$ model systems: (A) Fe(P)(PhNO)-(1-MeIm) and (B) Fe(P)(O$_2$)(1-MeIm). Note that $V_{33}$ (i.e., $V_{zz}$) is in the porphyrin plane in both cases.

**Table 7.** Optimized Structural Parameters for Oxy-Heme Model Systems[a]

| | $d$(Fe−O) (Å) | $d$(O−O) (Å) | ∠Fe−O−O (deg) | energy (au) | $\Delta E$ (kcal/mol) |
|---|---|---|---|---|---|
| A | 1.789 | 1.269 | 121.2 | −2667.60946695 | 3.81 |
| B | 1.781 | 1.268 | 120.2 | -2667.61541650 | 0.078 |
| C | 1.781 | 1.262 | 125.8 | -2667.61490064 | 0.40 |
| D | 1.787 | 1.270 | 121.4 | -2667.60968027 | 3.68 |
| E | 1.780 | 1.268 | 120.1 | -2667.61554189 | 0.00 |
| F | 1.791 | 1.261 | 126.0 | -2667.61020635 | 3.35 |

[a] G94/DFT B3LYP partial geometry optimization carried out by using a planar porphyrin, as described in the text, for the six molecules whose structures are shown in Figure 14. For comparison, the (unoptimized) picket fence porphyrin values are the following: $d$(Fe−O) = 1.750 Å; $d$(O−O) = 1.240 Å; ∠Fe−O−O = 131°. The basis sets used are the following: Fe Wachters/6-31G* C,N,O and 3-21G* H.

optimizations on protein fragments. In any case, all of the $\Delta E_Q$ calculations yield a value of ≈−2 mm s$^{-1}$, in very good agreement with the low-temperature Mössbauer experiments.

Since we were unable to reproduce the very small $\Delta E_Q$ suggested previously[14] we therefore need an alternative explana-

tion for the temperature dependence of the $^{57}$Fe Mössbauer quadrupole splitting. Fortunately, there are two additional pieces of information we can use. First, previous NMR measurements on oxypicket fence porphyrin have revealed very fast axial rotation of O$_2$ in the FeO$_2$ subunit,[11] and second, in oxymyo-

**Table 8.**   DFT Computed $^{57}$Fe Electric Field Gradient Tensor Elements and Mössbauer Quadrupole Splittings for Oxy-Heme Models[a]

| structure | electric field gradient (au)[b,c] | | | quadrupole splitting $\Delta E_Q$ (mm/s) |
|---|---|---|---|---|
|  | $V_{11}$ | $V_{22}$ | $V_{33}$ |  |
| planar, unoptimized |  |  |  |  |
| A | −0.8417 | −0.7734 | 1.6150 | −2.62 |
| B | −0.7042 | −0.4332 | 1.1374 | −1.86 |
| C | −0.5898 | −0.3449 | 0.9346 | −1.53 |
| D | −0.8202 | −0.7395 | 1.5597 | −2.53 |
| E | −0.6958 | −0.4398 | 1.1356 | −1.86 |
| F | −0.8268 | −0.6883 | 1.5152 | −2.46 |
| optimized |  |  |  |  |
| A | −0.8337 | −0.7902 | 1.6238 | −2.63 |
| B | −0.7512 | −0.3704 | 1.1216 | −1.85 |
| C | −0.7762 | −0.3487 | 1.1249 | −1.86 |
| D | −0.8227 | −0.7925 | 1.6152 | −2.62 |
| E | −0.7391 | −0.3819 | 1.1210 | −1.85 |
| F | −0.8482 | −0.7124 | 1.5606 | −2.53 |
| ruffled, unoptimized |  |  |  |  |
| A | −0.7749 | −0.7450 | 1.5199 | −2.46 |
| B | −0.7470 | −0.3983 | 1.1453 | −1.88 |
| C | −0.7429 | −0.3852 | 1.1280 | −1.86 |
| D | −0.7678 | −0.7441 | 1.5119 | −2.45 |
| E | −0.7428 | −0.4046 | 1.1474 | −2.45 |
| F | −0.8692 | −0.7678 | 1.6370 | −2.65 |

[a] The basic geometric structures used, **A**−**F**, are shown in Figure 14. [b] Locally dense basis set scheme: Fe Wachters', 6-311++G(2d) for $O_2$ and 5N coordinated to Fe, 6-31G* for the others except H are 3-21G*. [c] The models were built by using either a planar porphyrin or a ruffled porphyrin (the latter based on the structure seen in Fe(TPP)(CO)(1-methylimidazole), ref 43). For the unoptimized geometries we used $d(O−O) = 1.24$ Å, $d(Fe−O) = 1.75$ Å and $\angle Fe−O−O = 131°$. The optimized values are given in Table 7.
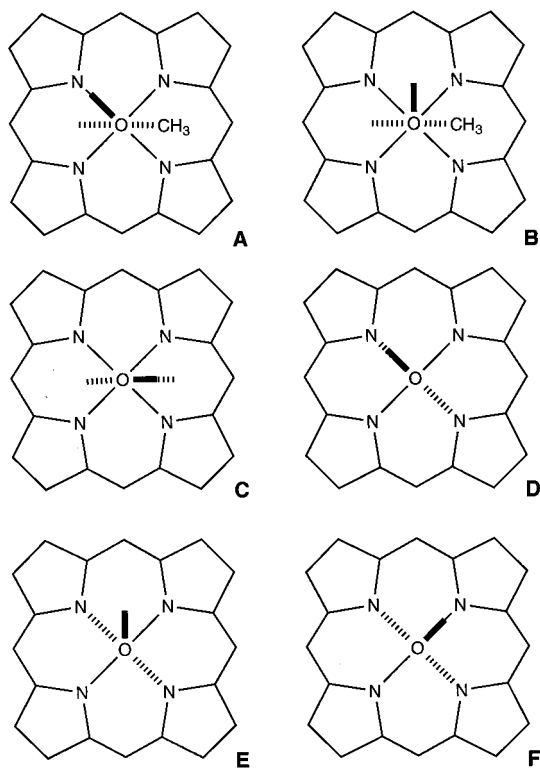


**Figure 14.**   Schematic illustration showing the six orientations of $O_2$ (solid line) and 1-methylimidazole (dashed line) with respect to the porphyrin macrocycle in Fe(P)($O_2$)(1-MeIm) used for DFT calculations.

globin, the $O_2$ molecule is crystallographically well-defined.[42] A quite reasonable general model for both model systems and proteins would therefore appear to be one in which in the model compound there is fast and complete axial rotation, or equivalently jumps between the low-energy conformers—just as found with CoNO in Co(TPP)(NO), and Co(OEP)(NO) at high temperature, and indeed as suggested as one possible model previously by Loew.[12] But in the proteins, the jumps would be

less frequent, and would only mix-in a small contribution from one of the rotameric states, consistent with the well-defined electron density for the FeO$_2$ unit in MbO$_2$,[42] and very large barriers to axial rotation as deduced from molecular mechanics simulations (data not shown).

Given that the EFG principal components have been calculated, we can predict the resultant motionally averaged EFG, basically as done by Spartalian et al.[14] For axial rotation, the in-plane tensor components ($V_{zz}$, $V_{xx}$; Figure 13) simply exchange and are averaged. For example, using mean $V_{zz}$, $V_{xx}$ tensor values (from Table 6) of −1.88, 0.67 mm s$^{-1}$ the average becomes $(−1.88 + 0.67)/2 = −0.61$ mm s$^{-1}$. As a result, the principal component is now perpendicular to the porphyrin plane, and has a value of 1.21 mm s$^{-1}$, which is very close to the 1.288 mm s$^{-1}$ (unsigned) value observed experimentally at high temperature with the picket fence system.[14] The DFT method therefore predicts not only the sign, magnitude, and orientation of the $^{57}$Fe EFG (or $V_{zz}$) at low temperatures but also the correct magnitude for $V_{zz}$ at high $T$, where motional averaging is known to be present − without use of any adjustable parameters. Given that DFT methods now correctly predict the EFGs in almost 20 compounds, including ∼10 metalloporphyrins, and that we find no evidence for a second site having a very small $\Delta E_Q$—even when more than a dozen possible geometries are investigated—we conclude that this simple motional model is correct, at least for the model system.

In proteins, the situation is more complex, at least for $O_2$. We have investigated the variable-temperature $^{57}$Fe Mössbauer spectra of Mb•PhNO, and we show these results, together with representative points from those reported previously by Parak for MbO$_2$, in Figure 15. As can be seen, the $^{57}$Fe $\Delta E_Q$ is essentially temperature independent with the PhNO complex, but is highly temperature sensitive in the case of MbO$_2$. Since the two species are isoelectronic, these results tend to rule out any "unusual" electronic effects as contributing to the $^{57}$Fe EFG, and in fact the simplest model to explain the differences between the two sets of EFGs would be one in which in Mb•PhNO the whole ligand is rigid, while in MbO$_2$, the ligand becomes
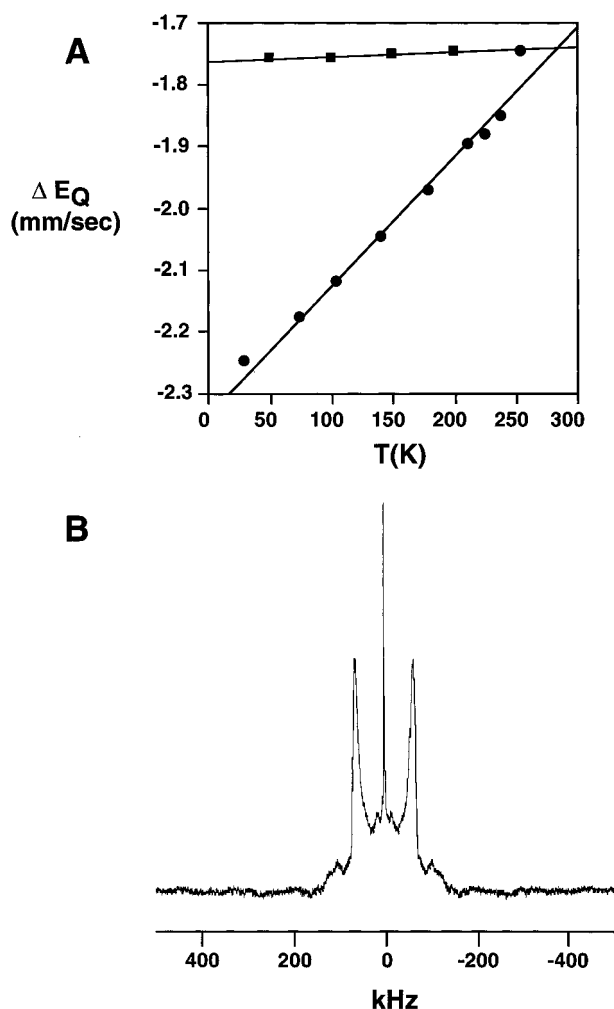
**Figure 15.** Graph showing Mössbauer and NMR results on heme proteins: (A) The effect of temperature on the Mössbauer quadrupole splitting, $\Delta E_Q$, for $MbO_2$ (●) and Mb•PhNO (■). The $MbO_2$ results are based on the values given in ref 15. (B) 8.45 T $^2H$ NMR spectrum of Mb•[$^2H_5$]-PhNO crystals at 298 K.

mobile, or at least partially so, on increasing temperature. There is strong support for this idea in the case of Mb•PhNO, where

as shown in Figure 15B the $^2H$ NMR spectrum of Mb•[$^2H_5$]-PhNO is characteristic of a rigid-lattice $^2H$ NMR powder pattern, even at 298 K. In the case of the $^{17}O$ NMR of Mb$^{17}O_2$ and Hb$^{17}O_2$, so far we have only been able to obtain $^{17}O$ spectra at 77 K (due to strong $H_2^{17}O$ overlaps and sensitivity problems at high temperatures), and the spectra are essentially the same as those obtained with oxypicket fence porphyrin at low temperature.[11] Nevertheless, a small (10−20%) contribution from a second FeO₂ orientation having essentially the same principal components, but rotated by 90° in the heme plane, will clearly cause a major decrease in $\Delta E_Q$, while maintaining the same basic Fe−O−O geometry. Thus, the same basic motional model appears to be able to explain both the model compound and metalloprotein results, using the DFT computed EFG tensor values and orientations. Unfortunately, however, the results of the calculations shown in Table 8 also indicate the possibility that both alternate O₂-substates and porphyrin ruffling could contribute to decreasing $\Delta E_Q$ in the proteins.

**Electrostatics.** With the availability of the results of accurate high-level DFT calculations, it becomes of great interest to investigate some of the other properties which then become available, and here, we focus on the electrostatic potential, $\Phi(\mathbf{r})$, mapped onto a charge density isosurface, $\rho(\mathbf{r})$. Obtaining a better understanding of the molecular electrostatic potential $\Phi(\mathbf{r})$ is of interest because it can be expected to lead to more detailed, quantitative descriptions of possible hydrogen bonding to CO and O₂, which is thought by many to be of importance in CO/O₂ discrimination in hemoglobin and myoglobin.[1] While the topic of charge distribution in FeO₂ and FeCO in proteins has been the subject of considerable debate over the years,[66] most studies have estimated what are essentially local, atomic-based charges, such as Mulliken populations or molecular electrostatic potential derived charges, which necessarily involve use of some model to deduce how to localize the charge. While this approach may be necessary in, for example, molecular mechanics methods, it would clearly be desirable to have a better understanding of the full potential surface, $\Phi(\mathbf{r})$, since this can in favorable cases be readily related to experiment. For example, Flaig and co-workers[37,38] have recently deduced the charge density, $\rho(\mathbf{r})$, as well as the electrostatic potential, $\Phi(\mathbf{r})$, for several amino acids, from high-resolution X-ray crystallographic data, and have shown that $\rho(\mathbf{r})$ and $\Phi(\mathbf{r})$, as well as the
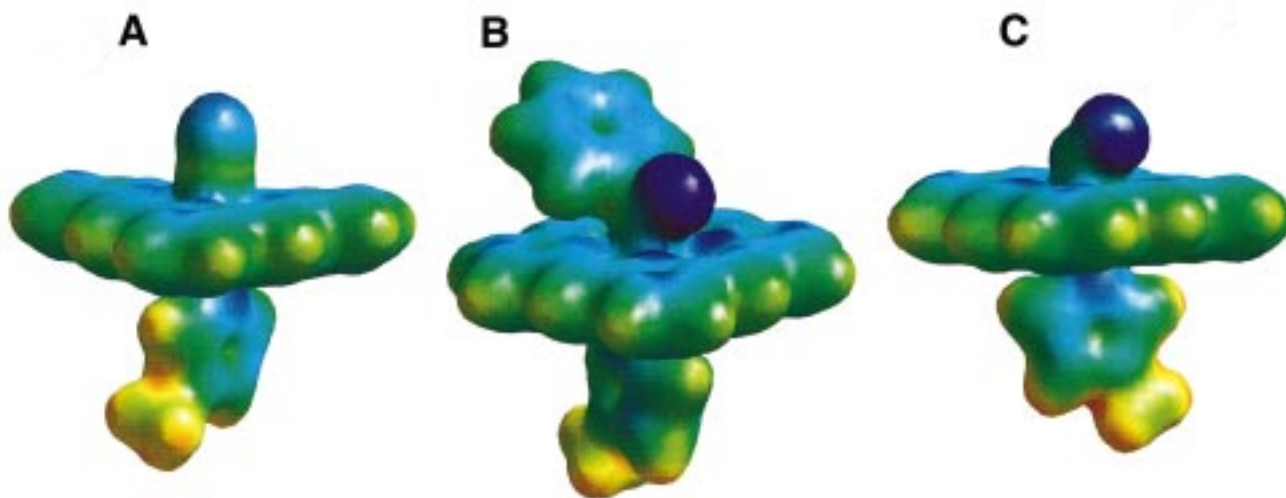


**Figure 16.** Electrostatic potential surfaces, $\Phi(\mathbf{r})$, mapped onto a 0.017 au charge density surface, $\rho(\mathbf{r})$, for (A) Fe(P)(CO)(1-MeIm), (B) Fe(P)-(PhNO)(1-MeIm), and (C) Fe(P)(O₂)(1-MeIm). The dark blue color in the case of O₂ and PhNO indicates a large negative electrostatic potential. The electrostatic potential on CO is −0.06 au on the carbonyl oxygen (in A) but −0.086 au in the oxy complex (in C), and −0.10 au in the PhNO adduct, (in B). The electrostatic potential surfaces are plotted for values between −0.06 and 0.17 au.

Laplacian of the charge density at bond critical points, $\nabla^2\rho(\mathbf{r})$,[39] are in excellent agreement with the results of high-level quantum chemical calculations. We have obtained similar results for asparagine and a small peptide,[73] which gives some confidence in the ability of modern DFT calculations to reproduce these electrostatic properties.

We therefore evaluated $\rho(\mathbf{r})$ and $\Phi(\mathbf{r})$ for three CO, PhNO, and $O_2$-containing metalloporphyrin models, and we show in Figure 16 $\Phi(\mathbf{r})$, $\rho(\mathbf{r})$ results in which the molecular electrostatic potential is mapped onto a charge density isosurface, for CO, PhNO, and $O_2$-containing metalloporphyrins. These results show that there is a clear distinction between $\Phi(\mathbf{r})$, the electrostatic potential, for bound CO and $O_2$, with the bound $O_2$ exhibiting a more negative potential, $-0.086$ vs $-0.06$ au. Also of interest is the observation that the electrostatic potential for the terminal oxygen in the PhNO adduct of $-0.10$ au is similar to that observed in the $O_2$ adduct, consistent with the isoelectronic nature of the two systems. These electrostatic potential results were essentially independent of the functional used. Also of note is the observation that the electrostatic potential for oxygen in the bound CO is essentially indistinguishable from that of the adjacent porphyrin atoms—an observation that would argue against any specific, strong hydrogen bonding to CO—in contrast to the situation found with the $O_2$ adduct, where quite clearly the oxygen is highly electronegative (as with PhNO) and able to selectively interact with H-bond donors, such as a proximal histidine or glutamine.

## Conclusions

The results we have obtained above are of interest for several reasons. First, the synthesis and structural characterization of a range of Fe•PhNO, CoNO metalloporphyrins is of interest because it helps the development of a model for metalloporphyrin distortion.[43] In addition, there are many structural similarities with respect to axial ligand orientation between $FeO_2$, FeRNO, and CoNO, reflecting their similar electronic structures, and validating their use in testing theoretical methods for predicting spectroscopic observables for $Fe-O_2$ and $Fe-O_2$ analogue systems. Second, we have obtained solid-state NMR and as appropriate Mössbauer spectra on these $FeO_2$-analogue systems, and used DFT methods to predict the experimental results with good success, validating the calculations. Third, we have used the same DFT methods to investigate the $Fe-O_2$ interaction in a metalloporphyrin and in oxymyoglobin (and oxyhemoglobin). The magnitude, sign, and orientation of the $^{57}Fe$ Mössbauer EFG tensor is correctly predicted for all low-temperature data, and a motional averaging model in which the $FeO_2$ rotates (as found for $FeO_2$ and CoNO metalloporphyrins by NMR) gives a $\Delta E_Q$ of 1.21 mm s$^{-1}$, versus the 1.288 mm s$^{-1}$ (unsigned) value seen experimentally with

model systems. In proteins, the rotational barriers are higher, but only a small contribution from a second rotamer (having essentially the same EFG principal components) can have a major effect on $\Delta E_Q$. However, these results alone are insufficient to rule out significant contributions from porphyrin ruffling and other geometric changes, in the case of the heme proteins. Finally, the results of molecular electrostatic potential calculations show that the electrostatic potentials for CO and $O_2$ are quite different, with the $O_2$ complex being much more negative (at oxygen) than in CO, consistent with a strong hydrogen-bonding propensity in proteins, with the PhNO results being similar to those seen with $O_2$. Overall, the ability of DFT methods to successfully predict the chemical shifts and shift tensors, as well as the $^{57}Fe$ electric field gradient tensors (the Mössbauer quadrupole splittings, signs, and orientations) gives confidence in the future use of these methods to probe in more detail structure and bonding in both model systems, and in metalloproteins themselves.

**Supporting Information Available:** Tables of crystal data, structure solution and refinement, atomic coordinates, anisotropic displacement parameters, hydrogen coordinates, bond lengths and angles, and torsion angles (PDF). X-ray crystallographic files, in CIF format, are also available through the Internet. This material is available free of charge via the Internet at http://pubs.acs.org.

JA9832820